F 3 Photoelectron Emission Spectroscopy [1]

Claus M. Schneider
Peter Grünberg Institut
Forschungszentrum Jülich GmbH

Contents

---

[1] Lecture Notes of the 43rd IFF Spring School "Scattering Methods for Condensed Matter Research: Towards Novel Applications at Future Sources" (Forschungszentrum Jülich, 2012). All rights reserved.

A Preliminary Note About This Lecture

Photoelectron spectroscopy has matured into an extremely versatile and powerful analysis technique. It permits access to a very wide variety of materials and their electronic structure, ranging from complex bulk structures down to free atoms. Consequently, there is an enormous wealth of results and interesting examples on different systems available, which are well worth being discussed. For good reasons, however, this lecture must focus on a few essential basics, novel aspects and a very personal selection of examples. For an in-depth study of photoemission spectroscopy and phenomena, the reader is referred to a number of excellent textbooks and review articles covering this field [1–5].

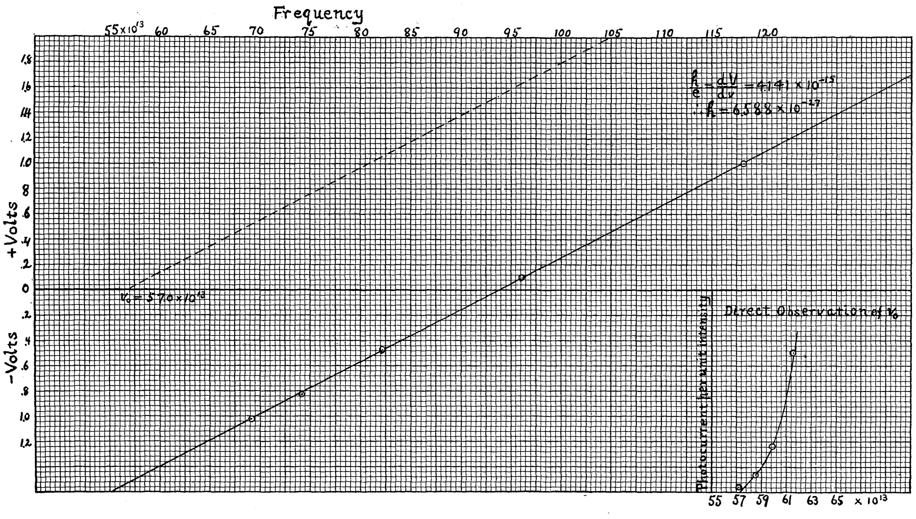

Figure 1: *Millikan's experiment on the photoelectric effect. For each exciting light frequency (data point) there is a well-defined maximum retarding voltage for the photoelectrons, the slope of the regression line yielding Planck's constant* h*. From [6].*

1 Introduction

The method of photoelectron emission spectroscopy goes back to the photoelectric effect, which was discovered by H. Hertz in 1887 [7] and refers to the phenomenon of electrons being ejected from a metal when illuminated by electromagnetic radiation. The explanation of the photoelectric effect by A. Einstein in 1905 [8] was one of the first triumphs of quantum mechanics. In his famous paper, Einstein extended Planck's quantum hypothesis by postulating that quantization was not a property of the emission mechanism, but rather an intrinsic property of the electromagnetic field. Using this hypothesis, Einstein was able to explain why the maximum kinetic energy E_{kin} of the emitted electrons varies with the frequency ν of the incident radiation as

$$h\nu = \Phi_0 + E_{kin} = \Phi_0 + \frac{1}{2}m_e v^2 \equiv eU \tag{1}$$

where h is Planck's constant, Φ_0 is a characteristic energy and called the work function, m_e, e and v denote electron mass, charge and velocity, respectively. This is exactly the result expected if photons are quantized with energies $h\nu$, and earned Einstein the 1922 Nobel prize in physics.

In the early photoemission experiments one basically determined the total photoelectron current $I_p(U)$ on a counter electrode as a function of a retarding voltage U. In this way, the maximum kinetic energy of the photoelectrons was determined from the condition $I_p(U) \Rightarrow 0$ (Fig. 1). From today's perspective this approach corresponds to an angle-integrated photoemission experiment [1].
The development of photoelectron spectroscopy started at the end of the 1950's with K. Siegbahn, who studied the energy levels of core electrons in atoms using excitation with x-rays [9]. Since the exact binding energy position of the core level depends on the chemical environment of the atom from which the photoelectron is emitted, Siegbahn coined the name Electron Spectroscopy for Chemical Analysis (ESCA) for this spectroscopic technique. He was awarded the physics Nobel prize in 1981 for his contributions to high-resolution electron spectroscopy.

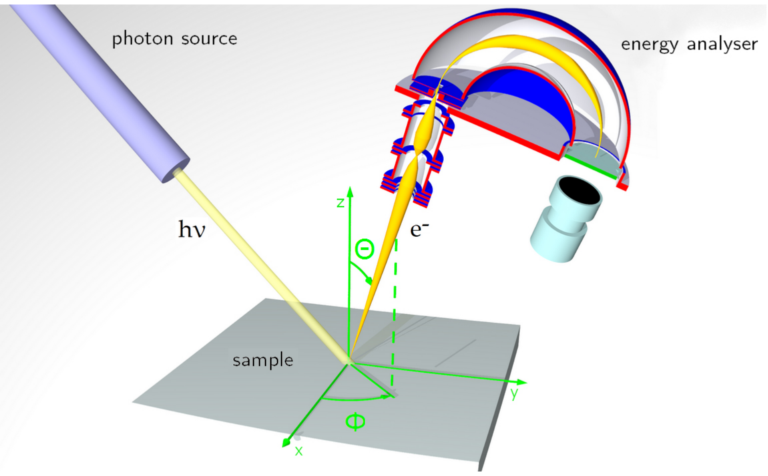

Figure 2: *Schematical picture of a modern photoemission experiment.*

A typical angle-resolved photoemission experiment as of today is sketched in Fig. 2. The photon source is typically a synchrotron radiation facility, which provides light over a broad range of photon energies $h\nu$ from the ultraviolet up to hard x-rays [10]. This light beam can be finely focused down to about 100 $\mu\mathrm{m}$, its direction of incidence onto the sample and its degree and orientation of polarization (linear, circular) can be precisely controlled. The electron energy analyzer is equipped with an electron optical entrance lens system, which defines the angular range of the photoelectrons analyzed. Therefore, the emission direction denoted by the angles (θ, ϕ) is a free experimental parameter. On the one hand, for solid state experiments, mostly single-crystalline samples are investigated under ultrahigh vacuum conditions ($p < 10^{-8}\mathrm{mbar}$). On the other hand, studies in catalysis require almost atmospheric pressure a the sample. This can be nowadays enabled by special designs of the entrance lens system involving differential pumping stages [11].

2 Fundamental Aspects of Photoemission

The valence electronic structure of a solid – in principle – can be calculated by solving a Schrödinger (nonrelativistic approximation) or Dirac equation (relativistic interactions included) for the respective lattice structure. For most metallic systems with weak electronic correlations, i.e. being close to the limit of a homogeneous electron gas, a quite successful description has been achieved within the framework of density functional theory (DFT) using the local density

(LDA) or more general local spin density approximation (LSDA) for the exchange-correlation potential [12]. In order to discuss the salient features of the photoemission process, we will first adopt this effective single-particle picture, although we must be aware of the fact that it does not capture electronic correlations properly.

One important result of the theoretical treatment is that the quantum mechanical wave function describing an electronic state in the solid depends on the symmetries of the Hamiltonian (e.g. lattice symmetries, inversion symmetry, time reversal symmetry, etc.) and must include also the electron spin. In the single particle picture the Hamiltonian can be written as

$$\begin{aligned}\left(\left[\tfrac{1}{2m}\left(\vec{p}-\tfrac{e}{c}\vec{A}\right)^2+eV(\vec{r})\right]+i\tfrac{e\hbar}{4m^2c^2}\vec{E}\cdot\vec{p}-\tfrac{e^2\hbar}{2mc}\vec{\sigma}\cdot\vec{B}-\right.\\ \left.-\tfrac{e\hbar}{4m^2c^2}\vec{\sigma}\cdot\left(\vec{E}\times\vec{p}\right)\pm eV_{exc}^{\uparrow\downarrow}(\vec{r})\right)\phi=E_{nls}(\vec{k})\phi.\end{aligned} \tag{2}$$

with ϕ and $E_{nls}(\vec{k})$ denoting the single electron wave function and energy eigenvalue, respectively. The terms in square brackets in eq. 2 represent the Hamiltonian of a system subjected to an electromagnetic field (vector potential $\vec{A}$). This part contains all crystalline symmetries through the potential $V(\vec{r})$. The Darwin term ($\sim \vec{E}\cdot\vec{p}$) may be understood as a relativistic correction to the electron energy. The fourth term contains the interaction of the spins – described by the Pauli spin matrices $\vec{\sigma}$ – with an external magnetic field $\vec{B}$. The last two terms contain the spin-dependent interactions through spin-orbit coupling and the exchange-correlation potential $V_{exc}^{\uparrow\downarrow}(\vec{r})$. The latter is responsible for the formation of spontaneously ordered magnetic states in solids. All spin-dependent terms in the Hamiltonian tend to reduce the symmetry of the system in one way or the other, leading to the splitting and hybridization of degenerate states. A full set of energy eigenvalues obtained from the DFT treatment forms a band structure $E_n(\vec{k})$ of the solid with the band index n and the electron wave vector $\vec{k}$. The wave functions are Bloch functions and are further classified by the orbital momentum quantum number ℓ and the spin quantum number s. Formally, the respective states may be written as $|n,\ell,\vec{k},s\rangle$ with their energy eigenstates $E_{nls}(\vec{k})$.

In addition to this valence electronic states comprising delocalized electrons, the full electronic structure of a solid also contains atomic-like localized core levels at higher binding energies $E_B \gtrsim 30$ eV (the binding energy is referred to the Fermi energy, i.e. $E_B = 0$ at E_F). In the ground state, the core states are completely occupied, whereas the valence states are occupied up to the Fermi energy E_F in the case of metals. In semiconductors and insulators the Fermi level lies in a band gap and the intrinsic bulk states are occupied only up to the valence band edge in the undoped case. At semiconductors band bending and surface photovoltage phenomena occur, which complicate the intepretation of photoemission results from semiconductors [13]. They will not be treated in this contribution.

Irradiating such an electronic structure with photons leads to excitation of electrons from occupied into unoccupied states in the electronic structure. If these empty states are located above the vacuum level E_{vac} of the solid, photoelectrons can leave the crystal and can be measured by an electron spectrometer, yielding characteristic signatures of the valence electronic states and core levels (Fig. 3). The quantum mechanical essence of the photoexcitation process is captured in Fermi's Golden Rule, which describes the transition probability between two electronic levels $|i\rangle$ and $|f\rangle$ with binding energies E_i and E_f, respectively:

$$P_{i\to f}=\frac{2\pi}{\hbar}\left|\langle f|\,\mathcal{O}\,|i\rangle\right|^2\delta(E_f-E_i-h\nu) \tag{3}$$

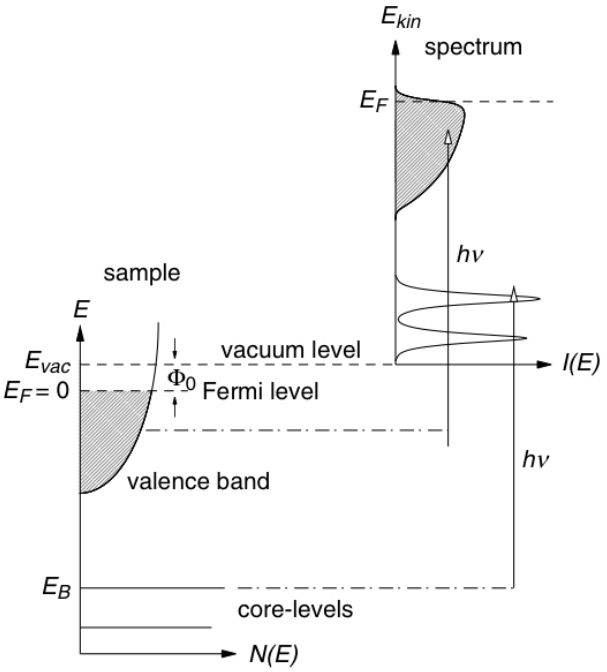

Figure 3: *Principle of the photoemission process. The electrons excited into states above the vacuum level form a photoelectron spectrum reflecting a broad valence electronic distribution (shaded area) and sharp emission lines from the core levels. From [3].*

In the simplest approach, the two levels $|i\rangle$ and $|f\rangle$ may be taken from the ground state electronic structure of the solid – which neglects the role of electronic correlations in the excitation process, as we will see below. The most important quantity in eq. (3) is the transition matrix element

$$M_{fi} = \langle f|\, \mathcal{O}\, |i\rangle \tag{4}$$

which essentially depends on the symmetries of the electronic wave functions and the photonic operator $\mathcal{O}$, whereas the delta function ensures energy conservation in the excitation process. For low photon flux densities the operator $\mathcal{O}$ can be treated within linear response theory and takes the form

$$M_{fi} = \frac{-e}{mc} \langle f|\, \vec{A}(\vec{r}) \cdot \vec{p}\, |i\rangle \tag{5}$$

with $\vec{A}(\vec{r})$ the vector potential of the electromagnetic field and $\vec{p}$ the momentum operator. It is usually assumed that the wavelength of the electromagnetic field is large compared to interatomic distances, i.e. $\vec{A}(\vec{r})$ varies only marginally in the spatial region contributing to the transition matrix element [1]. This view is commonly known as *dipole approximation* and simplifies the transition matrix element to

$$M_{fi} = \frac{-ie}{\hbar c} A_0 (E_f - E_i) \langle \psi_f|\, \vec{e}\cdot\vec{r}\, |\psi_i\rangle \tag{6}$$

with the complex amplitude of the vector potential A_0, its polarization vector $\vec{e}$, and the wavefunctions of the final and initial states ψ_f and ψ_i, respectively. This form of the transition matrix element is extremely valuable, as the quantity $\langle \psi_f|\, \vec{e}\cdot\vec{r}\, |\psi_i\rangle$ can be evaluated for selected symmetries of the wave functions and yields dipole selection rules, which are very useful for a

---

[1] This assumption should be revisited, if we go to photoexcitation with hard x-rays.

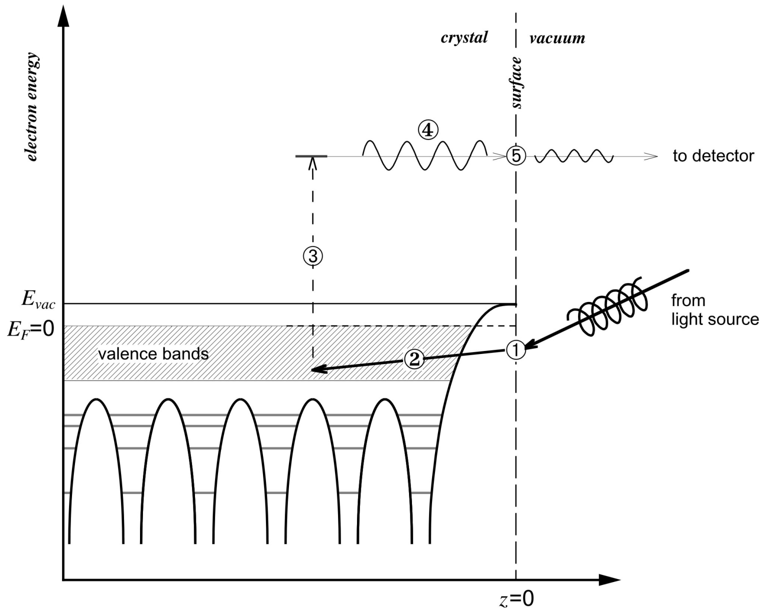

Figure 4: *Schematial representation of the three step model. The numbers denote: (1) refraction of the electromagnetic wave at the surface, (2) penetration of the photon into the solid, (3) photoexcitation, (4) propagation of the photoelectron to the surface, and (5) diffraction of the electron wave at the surface.*

qualitative interpretation of photoemission spectra. This can be most easily seen for atomic levels, the wavefunctions of which can be expressed in terms of a radial part and a part containing spherical harmonics $Y_{l,m}$. As the operator $\vec{e}\cdot\vec{r}$ can also be represented in terms of spherical harmonics (e.g. $Y_{1,0}$ for linearly polarized light, or $Y_{1,\pm m}$ for circularly polarized light), the matrix element $\langle\psi_f|\,\vec{e}\cdot\vec{r}\,|\psi_i\rangle$ can be fully calculated by evaluating products of spherical harmonics. The particular mathematics of spherical harmonics allows the matrix element to be nonzero only for particular relations between l_f, l_i, m_f, m_i, which is the basis of the selection rules. Although being only strictly valid for atomic systems, this approach has also been successfully extended to approximately describe the behavior of electronic states at high symmetry points in solids. A more general treatment of dipole selection rules in solids has been developed on the basis of group theory [1].

It is useful to recall that the photoexcitation is only part of the entire photoemission process. Once the electron has been excited into the upper level – which takes place on a timescale of 10^{-15} s – we call it a photoelectron. However, this highly energetic or "hot" photoelectron must find a way to leave the crystal, which is only possible if the excitation occurs into states above the vacuum level E_{vac}. The proper quantum mechanical treatment of the photoemission process is the so-called *one-step model,* which – at least in principle – permits a quantitative interpretation of photoemission spectra. However, a more intuitive access to the underlying physics is provided by the simpler *three-step model* which we will discuss in the following.

2.1 Three-Step Model of Photoemission

This model separates the photoemission of a single[2] electron into subsequent processes dealing with (i) the *photoexcitation*, (ii) the *transport* of the hot electron to the surface, and (iii) the *transmission* of the electron through the surface into the vacuum (Fig. 4). On a quantum me-

---

[2] This single-electron picture is convenient, because it allows in many cases a qualitative interpreation of photoemission spectra on the grounds of band structure calculations within the framework of density functional theory. It neglects, however, electronic correlations in the electronic structure which can be significant in certain materials or materials classes.

chanical level these steps have to be connected in a suitable way in order to allow the electronic wave function to propagate from one step to the next.

2.1.1 Photoexcitation

We have already mentioned above that the central aspect in the photoexcitation step concerns dipole selection rules. These rules predict allowed electronic transitions based on the symmetry of the electronic wave functions involved. In an atomic picture, these selection rules take the form:

$$\Delta L = \pm 1 \tag{7}$$

$$\Delta m_L = 0, \pm 1 \tag{8}$$

The photon carries an amount of angular momentum of $|L| = 1$ with it's polarization state being determined by $m_J = 0$ (linear polarization) and $m_J = \pm 1$ (right- and left-hand circular polarization, respectively). Linearly polarized light can be represented as a superposition of right- and left-hand circularly polarized waves. To illustrate the action of these selection rules we take the example of the excitation of an atomic $2p$ level. According to Eq. (11) we will find two types of allowed transitions, which may contribute to the photoemission spectrum

$$p \rightarrow \begin{cases} d \text{ for } \Delta L = +1 \\ s \text{ for } \Delta L = -1 \end{cases} \tag{9}$$

For the evaluation of Eq. (8) it is useful to consider that atomic states are usually subject to spin-orbit coupling, which leads to a characteristic splitting of the atomic levels and leaves only the total angular momentum $J = L + S$ as a good quantum number. Consequently, our p-level splits into a $p_{3/2}$ and a $p_{1/2}$ state and with linearly polarized light, we will have allowed transitions of the type

$$\begin{array}{ccc} p_{3/2} & \rightarrow & d_{3/2} \\ p_{1/2} & \rightarrow & s_{1/2} \\ p_{-1/2} & \rightarrow & s_{-1/2} \\ p_{-3/2} & \rightarrow & d_{-3/2} \end{array} \tag{10}$$

whereas circularly polarized light gives us

$$\begin{array}{ccc} p_{3/2} & \rightarrow & d_{5/2} \\ p_{1/2} & \rightarrow & d_{3/2} \\ p_{-1/2} & \rightarrow & s_{1/2} \\ p_{-3/2} & \rightarrow & s_{-1/2} \end{array} \text{ for } (\Delta m_L = +1) \quad \text{and} \quad \begin{array}{ccc} p_{3/2} & \rightarrow & s_{1/2} \\ p_{1/2} & \rightarrow & s_{-1/2} \\ p_{-1/2} & \rightarrow & d_{-3/2} \\ p_{-3/2} & \rightarrow & d_{-5/2} \end{array} \text{ for } (\Delta m_L = -1) \tag{11}$$

Note that the dipole operator of the light acts only on the orbital part of the electronic wave function, i.e. on the spatial symmetries, but it cannot interact with the electron spin S directly. However, because spin-orbit coupling ties the spin to specific orbitals, a selective excitation can yield spin polarized photoelectrons even from nonmagnetic materials. This phenomenon is called optical spin-orientation [14] and is also the basis of all magnetodichroic effects observed in photoabsorption and photoemission [15]. In order to see how this works let us have a closer look at the $p \to s$ transitions described by Eq. (11) (selection rules for crystalline symmetries see Appendix). The states $s_{1/2} \equiv |\uparrow\rangle$ and $s_{-1/2} \equiv |\downarrow\rangle$ may be regarded as pure spin states. For positive light circularity we have transitions starting at $p_{-3/2}$ and $p_{-1/2}$. Usually, the probabilities for the two transitions - which can be simply calculated from the Clebsch-Gordon coefficients [16] - differ by a factor of 3, i.e. the amount of photoelectrons excited into $s_{-1/2}$ is 3 times that for the $s_{1/2}$ state. If we assume that we have a nonmagnetic situation, the $s_{-1/2}$ and $s_{1/2}$ states will be energetically degenerate and a summation over the two photocurrent contributions will yield a spin polarization of the photoelectrons of $P = -50\%$. The same treatment for negative light circularity yields $P = 50\%$, i.e. a reversal of the circularity also reverses the sign of the photoelectron spin polarization. This optical spin-orientation effect in the $p \to s$ transitions is particularly exploited in spin-polarized GaAs photocathodes [17], but it can also be observed as a general photoemission phenomenon in basically all materials.

The quantity measured in the photoemission experiment is a photocurrent $I(h\nu)$, which is composed by transitions between all possible initial (i) and final states (f)

$$I(h\nu) \sim \sum_{i,f} |\langle f|\, \mathcal{O}\, |i\rangle|^2\, \delta(\epsilon_f - \epsilon_i - h\nu) \tag{12}$$

Note that in this single particle picture the photoemission spectrum is represented by a series of sharp lines, which is not what is observed in the experiment. The reason of this discrepancy is the many-electron nature of the photoemission process, which will be discussed in sect. 2.3.

Once the photoelectron has been excited into the upper state it will propagate through the solid with a kinetic energy of $E_{kin} = h\nu - E_B$ according to energy conservation. The propagation direction is determined by the electron momentum $\hbar\vec{k}$, i.e. the electron wave vector $\vec{k}$ inside the crystal, which in turn is determined by a wave vector conservation law $\vec{k}_f = \vec{k}_i + \vec{q} \pm \vec{G}$. The relation between initial and final state wave vectors $\vec{k}_f$, $\vec{k}_i$ and the photon momentum $\vec{q}$ is given modulo a reciprocal lattice vector $\vec{G}$. In most cases, we can therefore focus our considerations on the photoemission spectra to the first Brillouin zone. For low photon energies well below 1000 eV the photon momentum can be safely neglected and particularly with respect to electronic band structures one then may assume *vertical* transitions, directly connecting the initial and final state. For higher photon energies, however, the photon momentum may become a crucial quantity.

2.1.2 Propagation

Inelastic mean free path – The propagation of the hot electron is captured in the second step of the three-step model. It takes into account that due to the strong Coulomb interaction in a solid the hot electron will suffer very efficient elastic and inelastic scattering processes, which affect both the energy and angular distribution of the photoemission spectrum observed outside the crystal. The main mechanisms are scattering due to electron-electron interactions and at defects. In particular, the inelastic scattering processes lead to a relaxation of the photoelectron towards the Fermi level. The effect of the inelastic scattering is usually discussed in the framework of an exponential damping of the photoelectron intensity along the path l

$$I(l) = I_0 \exp(-\frac{l}{\lambda_{in}}) \tag{13}$$

and is generally taken into account by the quantity λ_{in}, the *inelastic mean free path* (IMFP). The concept of the IMFP is essential to describe the finite information depth in a photoemis-

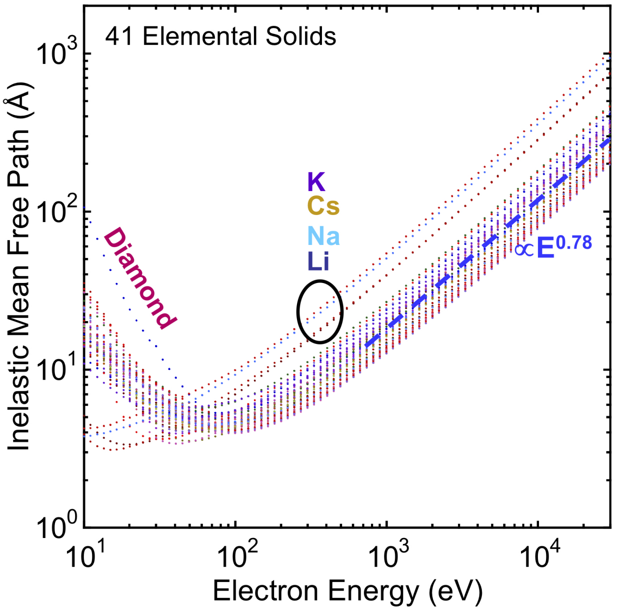

Figure 5: *IMFP values for 41 elements, calculated using the TPP-2M formula: Li, Be, three forms of carbon (graphite, diamond, glassy C), Na, Mg, Al, Si, K, Sc, Ti, V, Cr, Fe, Co, Ni, Cu, Ge, Y, Nb, Mo, Ru, Rh, Pd, Ag, In, Sn, Cs, Gd, Tb, Dy, Hf, Ta, W, Re, Os, Ir, Pt, Au, and Bi. Five "outlier" elements (diamond and the alkali metals) are included to illustrate the influence of the electronic structure characteristics. The dashed straight line for higher energies represents a variation as* $\lambda_{in} \sim E_{kin}^{0.78}$*, and is a reasonable first approximation to the variation for all of the elements shown. From [20].*

sion experiment. λ_{in} describes the average distance between two subsequent inelastic scattering events. This quantity is generally believed to follow a very similar behavior in different materials, which leads us to the well-known *universal curve* of the energy dependence of λ_{in}. A closer look, however, reveals that the curve is universal with respect to the general shape only. In quantitative respects the curve depends on the electronic structure of the element or material in question (Fig. 5).

Common to the IMFP curves is a minimum of λ_{in} of only a few Ångstroms at kinetic energies of ~100 eV and an increase towards both lower and higher energies. On this basis we can understand the high surface sensitivity of photoelectron spectroscopy at intermediate energies, which is both a virtue and a limitation. It can be – at least partly – overcome by exciting the photoelectrons with hard x-ray photons, i.e. photon energies of 6 - 10 keV (see Chapter 4.5). From Fig. 5 we see that at a kinetic energy of 10 keV the IMFP increases up to 10 nm. This energy-dependent variation of the information depth forms the basis for hard x-ray photoemission.

Photoelectron diffraction – While moving through the crystal the photoelectron can also be elastically scattered, giving rise to photoelectron diffraction (PD). This phenomenon is often also referred to as x-ray photoelectron diffraction (XPD) due to the higher excitation energies that are often used. In XPD a core-level photoelectron scatters from the atoms neighboring the emission site, so as to produce an angular anisotropy in the out-going photoelectron intensity [18]. The qualitative effects expected for the simple case of emission from the bottom atom in the diatomic molecule are shown in Fig. 6(a), and a quantitative calculation for emission from the C 1s subshell in an isolated CO molecule at 500 eV kinetic energy is shown in Fig. 6(b). Electron-atom elastic scattering is typically peaked in the forward direction, with this effect becoming stronger (that is, having a stronger and narrower forward peak) as energy increases [18]. For the CO case in Fig. 6(b), the intensity in the forward direction is in fact enhanced relative to that expected without scattering (I_0 in the figure) by about three times. Thus, one expects in XPD curves both a forward scattering peak (some-times referred to as forward focussing) along the interatomic direction, as well as higher-order diffraction interference effects that one can also consider to be holographic fringes. Back scattering is weaker as energy increases, but Fig. 6(b) shows that, even at 500 eV, there are still interference fringes in the backward direction.

Such XPD effects are very useful to determine the local atomic arrangement around an emitter atom. The XPD signals can be interpreted and modelled using the ingredients shown in Fig. 6(c). The polarization $\hat{\varepsilon}$ of the light influences the directionality of the initial photoelectron wave, and for emission from an s-subshell, the outgoing unscattered wave φ_0 has an amplitude proportional to $\hat{\varepsilon} \cdot \hat{k}$, where $\hat{k}$ is a unit vector in the direction of the photoelectron wave vector, and the photoelectron deBroglie wavelength will be given by

$$\lambda_e = h/|\vec{p}| = 2\pi/\left|\vec{k}\right|, \quad \text{in convenient units}: \ \lambda_e[\text{Å}] = \sqrt{150.5/E_{kin}[\text{eV}]} \tag{14}$$

Thus, an electron with 150 eV kinectic energy has a wavelength of about 1 Å, and a 1500 eV electron of about 0.3 Å, and these numbers are comparable to atomic dimensions. The outgoing photoelectron will elastically scatter from neighboring atoms j to produce wave components φ_j, and this process is describable in first approximation by plane-wave scattering, or more accurately by spherical-wave scattering. This scattering can be incorporated into a scattering factor f_j, which is furthermore found to be strongly peaked in the forward direction for energies above about 500 eV, as noted previously. The photoelectron wave components will also be

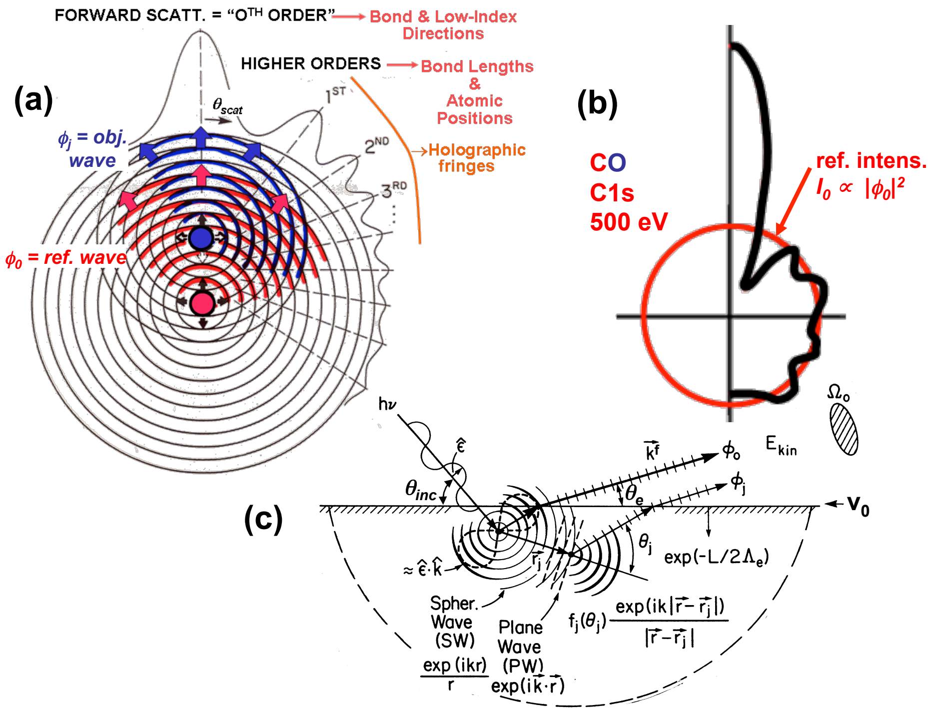

Figure 6: *Illustration of various aspects of photoelectron diffraction. (a) Simple diffraction features expected in emission from one atom in a diatomic system. (b) An accurately calculated diffraction pattern for C 1s emission from CO at a kinetic energy of 500 eV. Note the strong forward scattering peak, and other interference peaks or fringes extending from near the forward scattering direction to the backward scattering direction. (c) The basic theoretical ingredients required to describe photoelectron diffraction. From ref. [18], with calculations via ref. [19].*

inelastically attenuated as they traverses some total path length L in getting to the surface, with their amplitudes decaying as $exp(-L/2\Lambda_e)$. Finally, they will be refracted at the inner potential barrier V_0. Summing up all wave components (unscattered and scattered) and squaring then yields the diffraction pattern. Electrons can also be multiply scattered from several atoms in sequence, and accurate calculations of the resulting photoelectron diffraction patterns require including this for many cases, especially if scatterers are somehow lined up between the emitter and the detection direction, as along low-index directions in multilayer emission from a single crystal. Various programs are now available for calculating XPD patterns, with one web-based version being particularly accessible [19].

2.1.3 Transmission

In the final step of the three-step model the photoelectron has arrived at the surface and will leave the crystal. For this purpose, however, it has to pass through the surface potential barrier which matches the periodic potential inside the crystal to the vacuum outside. From simple quantum mechanics we know that an electron wave passing across a potential step Φ will be elastically scattered and diffracted, i.e. it will change its trajectory. In reality the surface potential barrier is not a step function, but smoothly varies as $\Phi(z)$. The details of the scattering process depend on the shape of $\Phi(z)$. The diffraction of the photoelectron in the surface potential is the reason that the wavevectors of the electrons inside the crystal $\vec{k}_{in}$ and outside in the vacuum $\vec{k}_{out}$ are not conserved. A conservation law exists only for the component parallel to the surface plane

$$k_{\|,in} = k_{\|,out} + G_{\|} \tag{15}$$

with $G_{\|}$ being a two-dimensional reciprocal lattice vector in the surface Brillouin zone. In order to relate the perpendicular component of the photoelectron wave vector $k_{\perp,out}$ to the electronic states inside the solid, more sophisticated methods for the band mapping have to be used [1]. The simplest one assumes the final electronic states to be described by a nearly-free electron parabola $E_f = \hbar^2 k_f^2/2m^*$ with an effective electron mass m^*. As the initial and final states are connected by vertical transitions in the band structure, k_f can be basically determined from E_f. This procedure fails, however, if the final state band structure deviates considerably from the nearly-free electron picture, which is the case particularly at hybridization regions. In this case, it is more reasonable to use final states from a band structure calculation for comparison. However, all these analyses will only yield a qualitative interpretation of the photoemission spectra. For a quantitative interpretation, a full photoemission calculation within a one-step model is needed.

2.2 One-Step Model of Photoemission

A considerable drawback of the three-step model is its limitation to a qualitative description of the photoelectron spectra. For a more quantitative description, first of all, the transition probabilities for all electronic excitations must be calculated on the basis of a realistic band structure for a semi-infinite system, for example, derived from density functional theory. The formalism must also take into account surface states or transitions into evanescent final states. Secondly, we must properly consider the multiple scattering events which the hot electron suffers in the final state. These are caused by the strong electron-electron interaction. This situation is more adequately described by the so-called one-step model, which considers the excitation and subsequent transport in a common framework. In particular, the multiple scattering of the electron waves in the surface-near region and in the surface potential is treated in analogy to formalisms developed for low energy electron diffraction (LEED). In LEED an electron wave enters the crystal and subsequently goes through a multiple scattering process. If we invert the order on the time scale, we retrieve our final state in the photoemission process, with the excited electron propagating towards the surface. This state is therefore also called a *time-reversed LEED state* [21]. In terms of kinetic energy there is a gradual transition from the LEED to the photoelectron diffraction regime. PED effects can therefore be included into one-step photoemission theories.

On the basis of one-step photoemission theories one arrives at a reasonable quantitative description of the photoelectron spectra. This may even include effects due to spin-orbit coupling and the electron spin, in which case a relativistic Dirac-type formalism is involved. In this way it becomes possible to calculate magnetic dichroism and spin polarization spectra.

2.3 Refinement of the One-Electron Model

2.3.1 Electronic correlations

In the above discussions we have always implicitely assumed that the electronic system under investigation can be modelled within an effective single-electron picture. This has the advantage that the features appearing in the photoemission spectra may be directly related to specific interband transitions in the electronic structure, involving band states or core levels. As we have seen in Part A of this book, however, the single-particle picture may fail to capture the essential physics of a system, because it may underestimate the correlations in a many-electron system. This is true for the entire family of so-called highly-correlated systems, which includes transition metal oxides and other materials exhibiting phenomena such as high-temperature superconductivity, colossal magnetoresistance or multiferroicity. Such systems are usually described by theoretical approaches beyond simple LDA, for example, LDA+U or dynamical mean field theory (DMFT). The interpretation of photoemission results from such systems is more involved and must take into account the influence of the electron-electron interactions in all steps of the photoemission process.

2.3.2 Spectral shape of photoemission lines

There is, however, a second way through which electronic interactions enter the photoemission experiment. According to Fermi's golden rule (eq. 3) the δ-function taking care of the energy conservation implies all photoemission signatures to be infinitely sharp lines. This should hold particularly for core level photoemission lines. Inspection of the schematical picture in Fig. 3 already reveals that the photoemission line will have a finite width. This is due to the multielectron character of the photoemission process itself.

Whenever a photoelectron is excited to the upper level, it leaves behind a hole in the lower level. Strictly speaking the photoemission process converts an N-electron system into an $(N-1)$-electron system, if the photoelectron has left the crystal, before the hole has been filled again. The photoelectron and the hole interact with each other through Coulomb interaction, which may lead to a renormalization of the binding energies, the appearance of spectral satellites, and a finite linewidth of the spectral line. This has two profound consequences. First, the terms ground and excited state become a different meaning, because they rather refer to an N and $(N-1)$ electronic system, respectively. Second, photoelectron spectroscopy always measures an excited state of matter rather than the electronic ground state. In a somewhat larger picture this is a nice illustration of one of the paradigms in quantum physics, according to which a measurement always affects and alters the system measured. Fortunately, modern condensed matter theory is able nowadays to handle many-electron systems both in the ground and excited state and can therefore provide a full photoemission calculation.

The role of electronic interactions in the photoexcitation spectrum is often taken into account within a Green function formalism [2]. The Green function $G(\vec{k},\epsilon)$ describes the behavior of a quasiparticle, which is "dressed" by the electronic correlations and the electron-hole interaction. Their influence is globally expressed by means of the complex self-energy Σ. Without going through the details of the formalism, from the Green function one can finally calculate the *spectral density function* $A(\vec{k},\epsilon)$, which may be compared to experimental results

$$A(\vec{k},\epsilon) = -\frac{1}{\pi}\mathrm{Im}G(\vec{k},\epsilon) = -\frac{1}{\pi}\frac{\mathrm{Im}\Sigma(\vec{k},\epsilon)}{[\epsilon-\epsilon_k-\mathrm{Re}\Sigma(\vec{k},\epsilon)]^2+[\mathrm{Im}\Sigma(\vec{k},\epsilon)]^2}. \tag{16}$$

A closer inspection of eq. 16 reveals that the real part of Σ introduces a renormalization of the energy ϵ_k of the spectral feature, whereas the imaginary part of Σ describes the finite lifetime of the quasiparticle state, resulting in a finite spectral width. As we will see below, the self-energy Σ can be conveniently employed to include further interactions, such as electron-phonon and electron-magnon coupling.

The spectral density function replaces the delta function in eq. 12. The total photocurrent is again determined by summing up over all dipole-allowed optical transitions between the many-electron states Φ_f and Φ_i weighted by the spectral density. We then arrive at the following description of the photocurrent [22]

$$\begin{aligned} I(h\nu) &\sim \sum_{f,i} |\langle\Phi_f|\,\mathcal{O}\,|\Phi_i\rangle|^2 A_{ii}(\epsilon_f-h\nu) \qquad (17)\\ &= \frac{1}{\pi}\sum_{f,i} |\langle\Phi_f|\,\mathcal{O}\,|\Phi_i\rangle|^2 \frac{|\mathrm{Im}\Sigma(\epsilon_i)|}{[\epsilon_f-\epsilon_i-h\nu-\mathrm{Re}\Sigma(\epsilon_i)]^2+[\mathrm{Im}\Sigma(\epsilon_i)]^2}. \end{aligned}$$

This is the basis for modern photoemission calculations, which attempt a quantitative interpretation of the experimental data.

3 Techniques

3.1 Electron Spectrometers

During the last decade, we have seen a considerable improvement in photoelectron spectrometer technology, mainly driven by the continuous quest for improved spectral resolution. By now, commercially available energy analyzers may be able to achieve an energy resolution below 1 meV [23]. The most common type of photoelectron spectrometers nowadays are display-type energy filters which are able to efficiently acquire intensity distributions over a certain range of angles and energies within a single measurement. An example for such a hemispherical display spectrometer is given in Fig. 7. The photoelectrons moving away from the sample surface are accepted by a lens system, which defines the angular spread, i.e. the $k_\parallel$ value transmitted. The hemispherical capacitor employed to disperse the electrons according to their kinetic energy is usually operated at a fixed pass energy E_{pass} in order to keep the energy resolution constant throughout a spectrum. The slit between the lens and the hemispheres separates the angular and energy information. The lens system therefore also has the task to accelerate/decelerate the electrons to the pass energy. After being dispersed in the electrostatic field a part of the electrons leaves the analyzer through a second aperture towards the areal electron detector. This usually comprises a combination of a multichannel plate (MCP) and position-sensitive read-out. The MCP consists of an array of narrow channels each being typical several 10 μm in diameter. In each channel a photoelectron is amplified by a factor of 10^4–10^6. This signal is then transported into the position-sensitive readout. The read-out may be a phosphor screen observed by an intelligent camera system which sorts and counts the events into a 3-D array in a computer.

Alternatively, there are resistive anode type detectors, which directly output voltage pulses to a multichannel analyzer. The specific design in Fig. 7 in fact features such a resistive anode arrangement called a delayline detector (DLD) [24] to make room for a second detector measuring the spin polarization of the photoelectrons (see below).

For specific purposes a wide variety of specialized electron spectrometers have been developed over the years. Most of them employ the electrostatic dispersion principle or a time-of-flight approach, in which the kinetic energy of the electrons is converted into a transit time along a defined trajectory. One of the challenges is to increase the angular acceptance of the analyzer in order to be able to capture a larger part of the photoelectron angular distribution in front of the sample. A very interesting design in this respect is the display-type spherical analyzer DIANA (Fig. 8) [25]. The electron trajectories emerging from the sample surface even at large emission angles are guided with high angular fidelity into the detector. The spectrometer is capable of

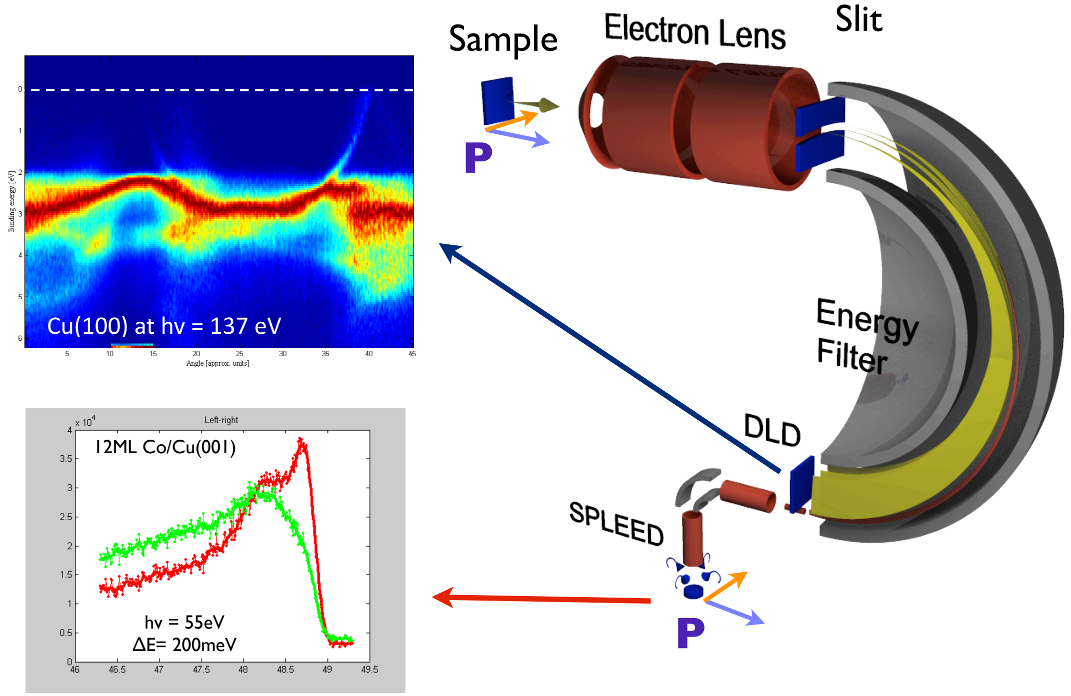

Figure 7: *Hemispherical photoelectron spectrometer with two-dimensional delayline detector (DLD) and SPLEED spin polarization analyzer operated at DELTA by the institute IFF-9.*

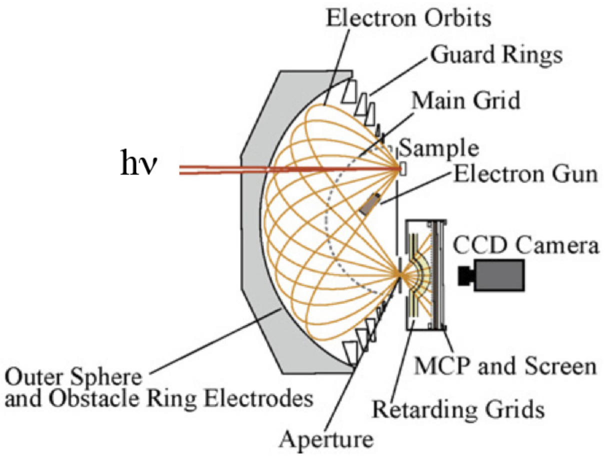

Figure 8: *Cross sectional scheme of the DIANA spherical capacitor spectrometer. The angular distribution of the photoelectrons is imaged onto a two-dimensional detector and captured by a CCD camera. From [25].*

mapping almost the entire half-space in front of the sample. This is particularly useful, for example, for photoelectron diffraction studies.

3.2 Spin Analysis

A "complete" photoemission experiment must analyze the photoelectron current with respect to all quantum numbers $|n, \ell, \vec{k}, s\rangle$. This includes also the electron spin, which carries important information about spin-dependent excitation and scattering processes in the solid. It can be shown that for an ensemble of electrons, the quantity spin can be expressed by a vector in real space, the spin polarization $\vec{P}$, the direction of which is defined by a quantization axis in the solid or the entire experiment [26]. Spin-dependent effects arise either through spin-orbit coupling or exchange interaction, the latter being a characteristic quantity in magnetic systems. Several types of spin polarization analyzers have been developed over the years . Their common principle of operation is based on the spin-dependent scattering of the photoelectrons off a target. The spin-dependence in the scattering process comes about by the same spin-dependent interactions mentioned above. In a simple picture, these interactions define a spin quantization axis and cause electrons with spin-up and spin-down to scatter with different probability into a direction perpendicular to this quantization axis. A counting detector placed in this direction will thus count different rates of scattered electrons for incident spin-up or spin-down photoelectrons, for example, $I^{\uparrow}(E)$ and $I^{\downarrow}(E)$. By subsequently orienting the spin-sensitive axis of the detector along the x, y, and z-axis, we can determine all three components of the spin polarization vector $\vec{P}(E)$.

There is only one spin polarization analyzer so far which is based on the exchange interaction. It involves low energy scattering ($E_s = 7$ eV) at a single-domain Fe(001) surface. Detectors exploiting spin-orbit coupling either involve high-energy Mott scattering at the atomic potential (several 10 keV up to 100 keV) or low energy scattering at the periodic potential of a solid (typically 100eV). Since the strength of the spin-orbit coupling increases with the atomic number Z, all spin-orbit scattering targets comprise heavy atoms, such as Au, W, or U.

In order to see how a spin detector is interfaced with the electron spectrometer, we choose the SPLEED detector as an example (Fig. 9). In this detector one effectively performs a $\underline{s}$pin-$\underline{p}$olarized $\underline{l}$ow-$\underline{e}$nergy $\underline{e}$lectron $\underline{d}$iffraction experiment [27]. The incoming electrons hit a W(001) surface at normal incidence with a scattering energy of about 104 eV. The diffracted beams cre-

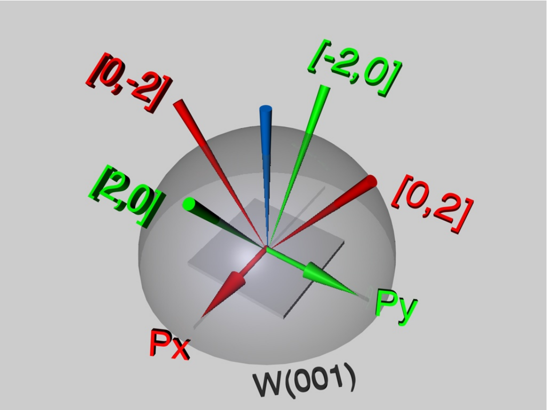

Figure 9: *Sketch of the SPLEED spin detection principle using a W(001) crystal. The spin polarization components P_x (red) and P_y (green) are measured simultaneously.*

ate a four-fold symmetric LEED diffraction pattern above the surface. Of particular importance are the $\{20\}$ diffraction beams, because they provide the highest spin sensitivity at these scattering conditions. Because of symmetry reasons the SPLEED detector is sensitive to two orthogonal components of the spin polarization vector. The components P_x and P_y are determined from the intensity of the LEED reflexes by

$$\begin{aligned} P_x &= \frac{1}{S} \cdot \frac{I_{[0,2]} - I_{[0,-2]}}{I_{[0,2]} + I_{[0,-2]}} \\ P_y &= \frac{1}{S} \cdot \frac{I_{[2,0]} - I_{[-2,0]}}{I_{[2,0]} + I_{[-2,0]}} \end{aligned} \tag{18}$$

with the spin sensitivity S. This procedure is repeated for every data point of the spectrum and yields a spin polarization spectrum $P_{x,y}(\vec{k}, E)$, which can be used to calculate the spin-up and spin-down contributions of one vector component to the photoemission spectrum according to

$$I^{\uparrow}(E) = \frac{I_0}{2}(1+ \quad P(E)) \quad \text{and} \quad I^{\downarrow}(E) = \frac{I_0}{2}(1 - P(E)) \tag{19}$$

with the spin-averaged total intensity I_0.

3.3 Spectromicroscopy

The instruments discussed so far are dedicated to very good energy and angular resolution, but they usually do not provide a significant lateral resolution. As a consequence, the studies are restricted to relatively large (mm) and homogeneous samples. However, the progress in nanotechnology leading to ever smaller structures and also the need to study inhomogeneous samples on small length scales is the driving force for a new class of instruments, so-called spectromicroscopes.

Basically, there are two different avenues, which are currently followed in parallel. In the scanning approach one uses a conventional electron spectrometer, but tries to focus down the light beam by means of zone plate optics or capillary optics. Depending on the wavelength of the light and the quality of the optical components, a minimum spot size of less than 50 nm seems to be within reach. This light spot is then raster scanned with respect to the sample, recording a spectrum at each location [28].

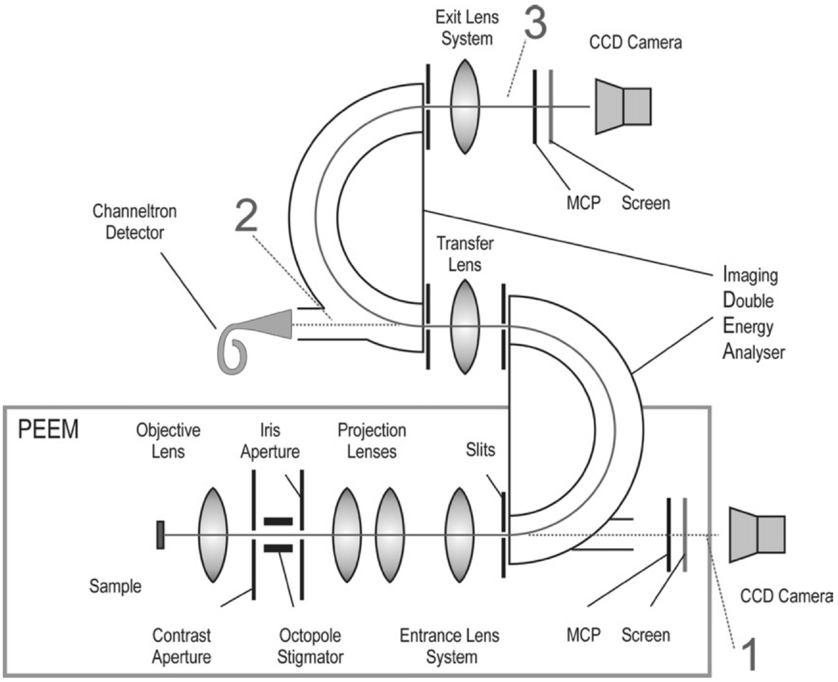

Figure 10: *Principle layout of the NanoESCA imaging spectrometer. From [29].*

In the full-field approach, the sample is illuminated by a more extended beam, and an electron-optical immersion lens microscope is used to image the surface in real time. This image is then passed through an energy analyzer, for example, an electrostatic one similar to the one discussed above. Behind the energy analyzer the now energy-filtered image is magnified onto the image detector, usually a MCP/phosphor screen unit with a slow-scan CCD camera. With these instruments, energy-filtered imaging with a resolution below 100 nm has already been shown. In Fig. 10 we show a different design which is employed in the NanoESCA instrument [29]. The energy filtering involves a system of two hemispherical analyzers connected by a transfer lens. The advantage of this layout is that imaging errors introduced by the first hemisphere are compensated by the second one, thereby improving the overall image quality. The instrument has three different imaging modes. The first one (1) takes the image from the PEEM column directly to the image detector. This corresponds to the normal unfiltered PEEM. The second operation mode (2) takes part of the electrons after the first hemisphere into a counting detector. The sample surface area where these electrons originate from is defined by means of an iris aperture and can be in the micrometer range. This mode is very interesting to measure small-spot spectra. Operation mode (3) corresponds to the energy-filtered imaging mode, i.e. the image is formed by electrons within a narrow energy window which can be adjusted, for example, to a particular core level photoemission line.

4 Selected Examples

In the following, we will discuss several examples illustrating different applications of photoemission spectroscopy covering band states and core levels.

4.1 Electronic and Chemical States

4.1.1 Valence state photoemission

The first example illustrates the mapping of the valence electronic states in a noble metal. A hemispherical display-type spectrometer like the one shown in Fig. 7 records an entire two-dimensional slice of the photoelectron distribution $E(\vec{k}_f)$ in front of the sample in a single measurement. For a Ag(100) surface, which is illuminated by photons with energy $h\nu = 35$ eV, such a slice is displayed as a colour-coded map in Fig. 11 for photoelectrons emitted around an angle $\theta = 20°$ with respect to the surface normal. The energy scale is renormalized to the Fermi energy E_F, and the photoelectron intensity is represented as a function of binding energy E_B and emission angle θ.

For a more detailed analysis of the spectral features one may take cuts through the $I(E_B, \theta)$ distribution, resulting in different types of spectra. A cut at fixed binding energy yields $I(\theta)$, which is sometimes called a *momentum distribution curve* (MDC). A cut at fixed angle yields $I(E_B)$, which is called an *energy distribution curve* (EDC) and corresponds to a "classical" photoemission spectrum.

Although the distribution in Fig. 11 somewhat resembles a band structure, it is important to note that the data are not a simple picture of the bands, because the energy and angular position of the intensity maxima is determined by the transition matrix elements and thus by the initial state and final state bands. Nevertheless, we can already clearly discern different types of spectral features with large and smaller dispersion. In fact, a comparison to bulk band structure calculations of silver along the [100] (Δ) direction reveals that the spectral structure that starts at the Fermi level and bends downwards to the right originates from a strongly dispersing band of symmetry Δ_1, which has a strong free-electron, *sp*-like character. The more localized 4*d*-like states in silver give rise to the strong almost horizontal lines at binding energies below 4eV.

The position of the maxima in the MCD's and EDC's can be used to precisely determine the initial electronic state in the band structure by different approaches [1]. Usually this procedure is repeated for different emission directions and surface orientations in order to map the position of the initial state bands throughout the entire Brillouin zone, or at least along high-symmetry directions. Fig. 12 displays such a result for copper, with the data points being obtained from

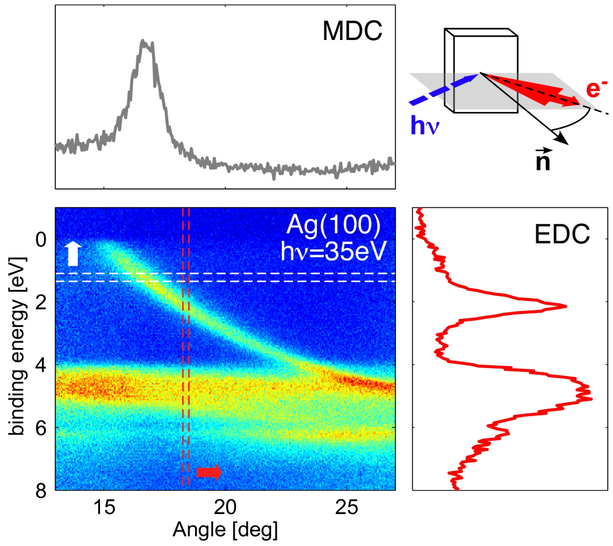

Figure 11: *Example of a two-dimensional $E(\theta)$ distribution recorded from an Ag(100) single crystal surface. The color code ranges from blue (no intensity) through yellow (medium intensity) to red (high intensity). Vertical and horizontal cuts through this distribution yield energy distribution curves (EDC) and momentum distribution curves (MDC), respectively. The broken lines bound areas of 5 lines on the detector which have been added up to the MCD (top) and EDC (right). Inset: Experimental geometry with the red triangle indicating the angular spread measured.*

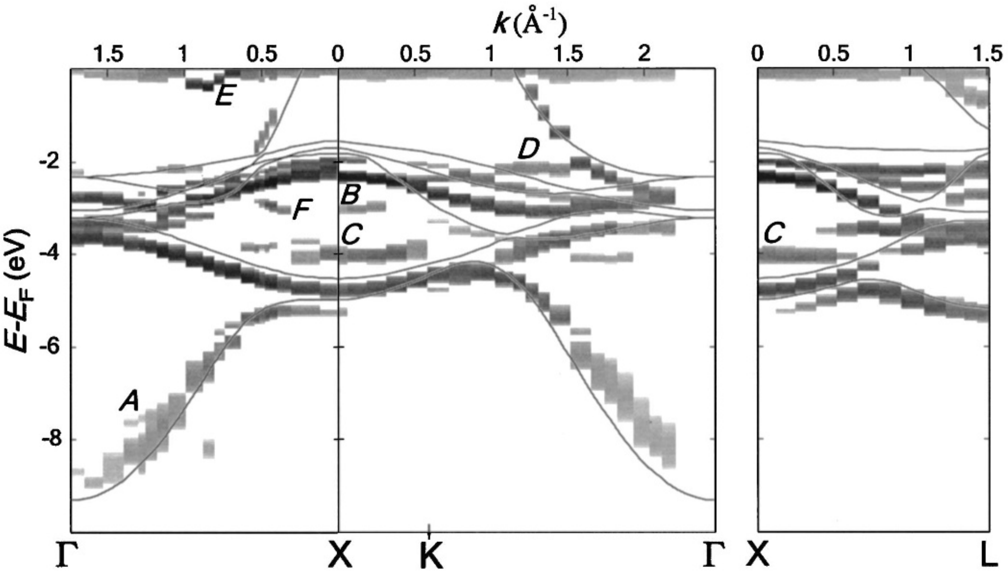

Figure 12: *Band mapping results for the bulk electronic states in a Cu single crystal along the [100]* $(\Gamma-\Delta-X)$*, ([110]* $(\Gamma-\Sigma-K)$*, and [111]* $(\Gamma-\Lambda-L)$ *directions. The bands are shifted from the DFT theoretical* $E(\vec{k})$*, shown by thin lines, due to excited-state self-energy effects. The constant line at* E_F *is due to the Fermi cutoff, and the peaks A–F are spurious structures due to multiple upper band composition, 1DOS maxima, and surface states. From [30].*

photoemission experiments and the lines representing a band structure calculation. The strongly dispersing bands starting at the Γ-point correspond to the free-electron like *sp*-type states. All other bands exhibit a weaker dispersion and have a strong *d*-type character, meaning that the electrons are more localized.

The band structure in Fig. 12 has been calculated within a relativistic scheme, i.e. it also contains the effects of spin-orbit interaction. Although copper is a material with low atomic number, spin-orbit coupling has been found to play an important role in the band symmetries, in particular, close to hybridization points. We also observe spectral signatures, which do not fit into the calculated bulk band structure $(A - F)$. A further analysis reveals that feature E is related to a surface state. The features B, C, and D are caused by transitions into regions with a strong one-dimensional density of states, where $k_\perp$ is not conserved. A hybridization of multiple upper bands leads to the appearance of feature A. Feature F is likely caused by surface state or surface resonance split off from the d bands [30]. We also note that the experimental data exhibit a systematic shift with respect to the calculated band. This is due to self-energy effects in the excited state.

4.1.2 Core level photoemission

The photoemission from the localized core levels gives rise to rather sharp spectral features at well-defined and characteristic binding energy values (cf. Fig. 3). These values are tabulated for the elements, for example, in the *X-Ray Data Booklet* [31], and range from several 10 eV for the shallow core levels up to 10 keV for the 1*s*-levels of heavy elements. Core level photoemission is often used to identify and quantify chemical species and is therefore also termed ESCA (Electron Spectroscopy for Chemical Analysis). For a sample consisting of one

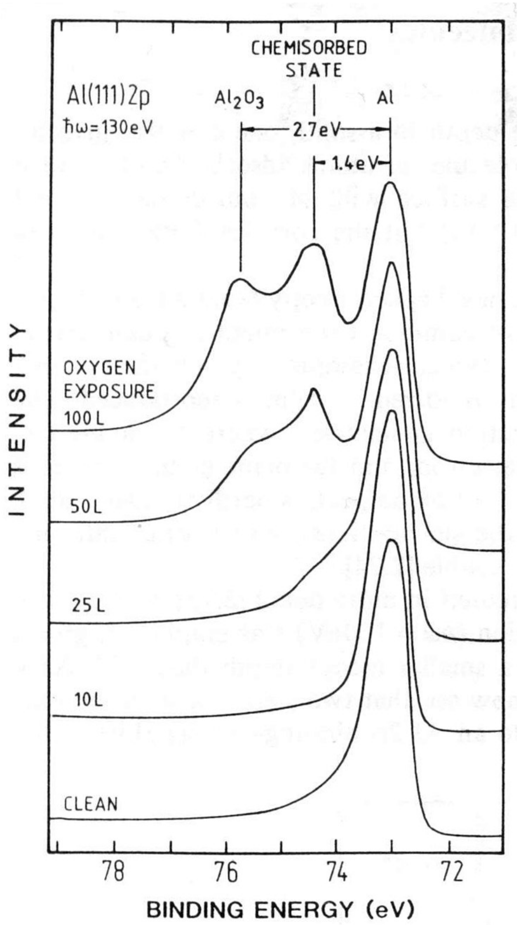

Figure 13: *Core level photoemission from Al(111). A surface reaction with oxygen leads to characteristic chemical shifts of the core level binding energies with respect to the clean surface. The amount of oxygen that the surface is exposed to is measured in units of Langmuir L* ($1L = 10^{-6} mbar \cdot s$)*. From [1].*

chemical element only, the binding energy of the spectral feature is sufficient to unambiguously identify the element[3].

An example is given in Fig. 13, which compiles different spectra recorded for the Al $2p$ core level. The bottom most spectrum has been obtained from a clean Al(111) surface and shows the $2p$ core level peak located at a binding energy of $E_B = 73$ eV. A further inspection of the spectrum reveals that the spectral line has a finite width and an asymmetric shape. The line width is mainly determined by the lifetime of the core hole created in the excitation process and by the energy resolution of the electron spectrometer. The asymmetric line shape arises mainly due to the excitation of electron-hole pairs in the vicinity of the Fermi level. This corresponds to inelastic electron scattering of the photoelectron in the solid, effectively shifting some spectral weight to the low binding energy side of the peak. This asymmetric line shape may be modeled, for example, with the Doniach-Sunjic approach [32].

The binding energy of a given core level may change, as soon as we alter the chemical environment, for example, by a chemical reaction. Although the chemical bonds formed with an atom as a consequence of the reaction involve mainly the valence electrons, they may cause a charge transfer from or to that atom. This process modifies the electrostatic screening in the atom, ultimately resulting in a slight shift of the core level binding energy. These socalled *chemical* shifts form the basis of more elaborate ESCA approaches in determining the chemical composition

---

[3] Usually one measures several core level lines at different binding energies in order to increase the accuracy of the element analysis.

of complex alloys and compounds. An illustration for chemically induced core level binding energy shifts is given by the remaining spectra in Fig. 13. These spectra are obtained by exposing the Al(111) surface to different amounts of oxygen in successive steps. After an oxygen exposure of 25 L we start to see a weak spectral feature on the high binding energy side of the $2p$ level. After 50 L this feature has grown into a well-defined sharp peak $E_B = 74.4$ eV, which can be attributed to photoemission from Al surface atoms onto which oxygen has chemisorbed. In addition, a third peak starts to form at still higher binding energies. After dosing 100 L onto the Al(111) surface, this third signature at $E_B = 75.7$ eV has evolved into a clear peak, which can be attributed to photoemission from Al atoms bonded in an Al_2O_3 environment. We therefore see that the oxidation from metallic aluminium to alumina is accompanied by a chemical shift of the Al $2p$ core level by about $\Delta E_B = 2.7$ eV.

4.1.3 Fermi surface mapping

A particular aspect in modern photoemission spectroscopy is the so-called *Fermi surface mapping*. In order to see how this approach works, it is useful to recall that the data provided by the 2D display analyzers represent an intensity distribution $I(E, \vec{k}_{\|})$. The electron wavevector $\vec{k}_{\|}$ parallel to the surface is defined by the experimental geometry. By varying the emission angles θ and ϕ (cf. Fig. 2) one obtains a set of slices through reciprocal space for different vectors $\vec{k}_{\|} = (k_x, k_y)$ in the surface plane. This data set can be condensed into a three-dimensional representation $E(k_x, k_y)$. An example for angle-resolved photoemission from a W(110) surface is shown in Fig. 14. The picture combines a vertical cut $I(E, k_x, k_y = 0)$ through the surface Brillouin zone (SBZ) with a horizontal cut $I(E = E_F, k_x, k_y)$. The intensity distribution $I(E, k_x, k_y = 0)$ reveals a clear dispersion of band segments along the high symmetry directions $\bar{\mathrm{S}} - \bar{\Gamma} - \bar{\mathrm{S}}$ in the SBZ, which can be compared to appropriate band structure calculations. The horizontal cut $I(E = E_F, k_x, k_y)$ depicts a two-dimensional map of the electronic states

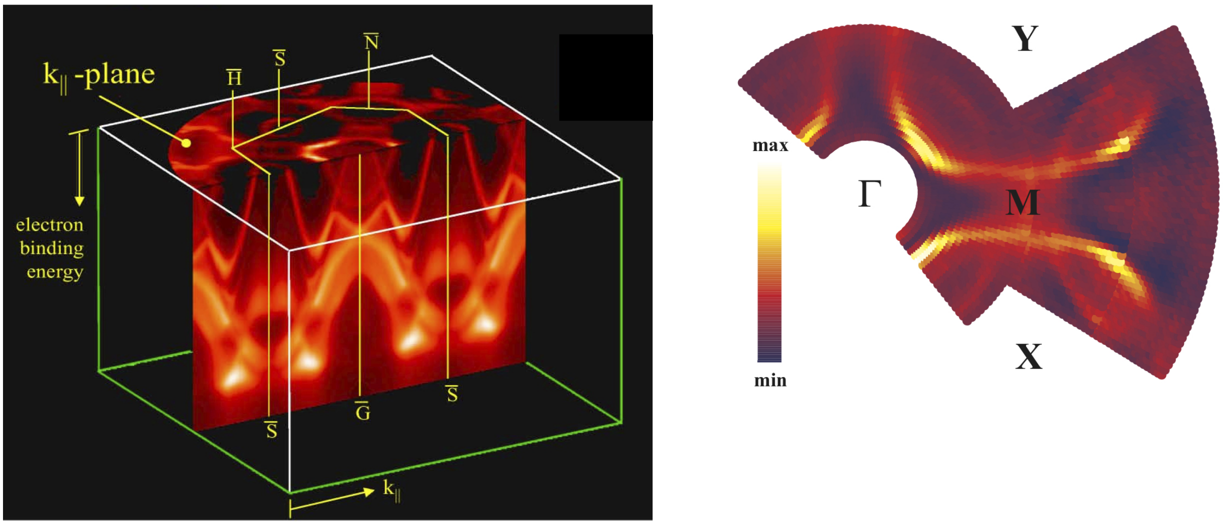

Figure 14: *(Right) Principle of Fermi surface mapping illustrated for photoemission from W(110). The plot compiles photoemission intensity distributions $I(E, \vec{k}_{\|})$ for different emission angles, which can be stacked in a three-dimensional scheme. A cut through the stack at $E = E_F$ yields a two-dimensional map of the Fermi surface in the plane defined by $\vec{k}_{\|}$. From [33]. (Left) Fermi surface for Pb-doped Bi2212, i.e. $Bi_2Sr_2CaCu_2O_{8-\delta}$. From [34].*

at the Fermi energy and can thus be *related* to the Fermi surface. In the interpretation we have to keep in mind that the map in Fig. 14 contains matrix element and photoelectron diffraction effects. These have to be taken into account when comparing the data to theoretical predictions.

The details of the Fermi surface are crucial in determining the physical properties of materials, for example, the magnetic anisotropy in magnetic systems or the origin of superconductivity. In fact, the onset of superconductivity is accompanied by the formation of a small gap around the Fermi level. It is for this reason that Fermi surface mapping has become a standard tool in the investigation of high-T_C superconductors (HTSC). The example in Fig. 14 depicts the Fermi surface of Pb-doped $Bi_2Sr_2CaCu_2O_{8-\delta}$ (short form Bi2212) [34]. The data have been recorded in the normal state (T=120 K) with a He discharge source ($h\nu = 21.2$ eV). The main Fermi surface is hole-like and has the form of tubes (rings) centered around the X, Y high symmetry points. In addition, weaker intensity features are observed specifically around the M point. This so-called shadow Fermi surface is attributed to a spin-related origin [34]. A detailed understanding of the Fermi surface and their change with temperature are mandatory to understand the microscopic mechanisms leading to HTSC.

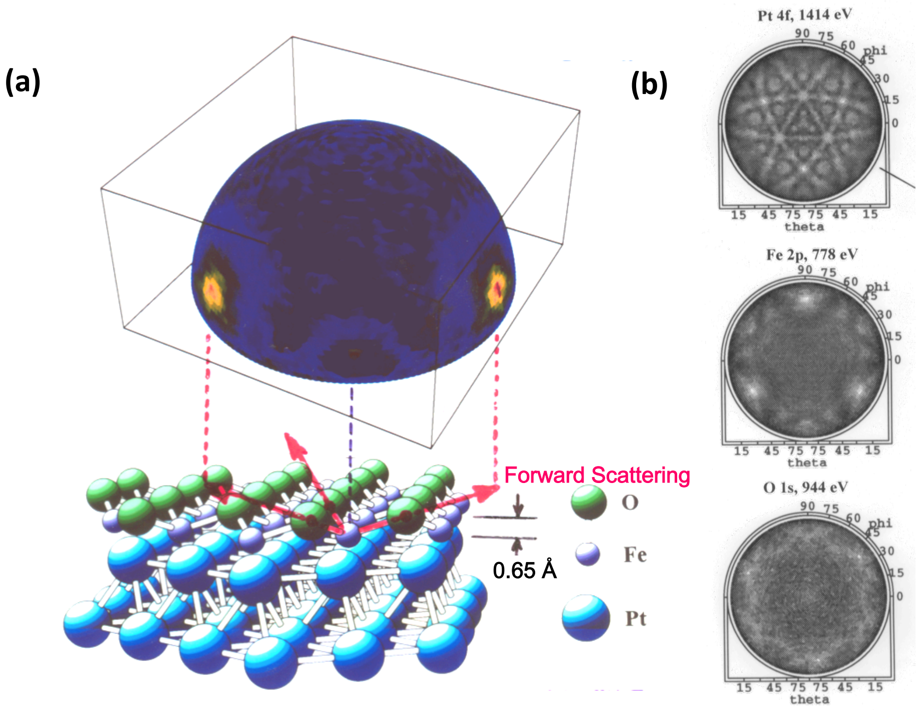

Figure 15: *X-ray photoelectron diffraction at 1486.7 eV excitation from a monolayer of FeO grown on Pt(111). (a) A full-hemisphere pattern for Fe $2p$ emission is shown, above the atomic geometry finally determined for this overlayer. (b) Diffraction patterns simultaneously accumulated for emission from Pt $4f$ (kinetic energy 1414 eV), Fe $2p$ (778 eV), and O $1s$ (944 eV). From Ref. [35].*

4.1.4 Photoelectron Diffraction

As one example of a photoelectron diffraction pattern, we show in Figure 15(a) the full hemisphere intensity distribution for Fe $2p$ emission at 778 eV ($\lambda_e = 0.44\ \mathring{A}$) from a monolayer of FeO grown on a Pt(111) surface [35]. At this energy, the forward-peaked nature of fj is observed to create strong peaks in intensity along the Fe-O bond directions. The angle of these peaks can furthermore be used to estimate the distance between the Fe and O atoms in the overlayer, and it is found to be only about half that for similar bilayer planes in bulk FeO, as illustrated in the bottom of Figure 15(a). Figure 15(b) also illustrates the element-specific structural information available from XPD. The Pt $4f$ XPD pattern from the same sample is rich in structure due to the fact that emission arises from multiple depths into the crystal, with forward scattering producing peaks and other diffraction features along low-index directions. The Fe 2p pattern is here just a projection onto 2D of the 3D image in Figure 15(a). The O $1s$ pattern shows only very weak structure, as the O atoms are on top of the overlayer, with no forward scatterers above them, and only weaker back scattering contributing to the diffraction pattern. Comparing the Fe and O patterns thus immediately permits concluding that Fe is below O in the overlayer, rather than vice versa. Other examples of photoelectron diffraction in the study of clean surfaces, adsorbates, and nanostructure growth appear elsewhere [18, 36].

4.1.5 Microspectroscopy

Chemical Information – Laterally resolving photoemission techniques can yield a two-dimensional distribution of the electronic and chemical states at the surface. The current challenge in microspectroscopy is the improvement of the spectral and lateral resolution in order to increase the image contrast and reduce the minimum feature size detectable. The example in Fig. 16 has been obtained with a NanoESCA instrument (cf. Fig. 10) and represents the current status of the field. The sample is a GaAs/AlGaAs layer stack comprising layers of different thickness, which has been cut into a cross section through the layer stacking (schematic stacking sequence in the center of the image). The image has been acquired with Ga *3d* core level photoelectrons excited with photons of 400 eV energy.

The image contrast arises from the different relative Ga concentration in the GaAs and AlGaAs layers and directly reflects the layer stacking. The AlGaAs regions appear darker than the GaAs areas. The stack included a number of double layer structures, which appear in the imaged cross section as pairs of parallel lines. These can be employed to determine the lateral resolution in the experiment. The two pairs on the right hand side of the image are clearly separated. For the remaining structures on the left-hand side, a line scan analysis across the lines is necessary to extract further information. We can see that the line pair denoted as P3 in the image cannot be separated anymore into two individual features. If one assumes a 20%/80% criterion for the lateral resolution Δx, we find a value of Δx=273 nm.

On the left hand side of the image, we can discern a single line of darker contrast. This signal originates from a single AlGaAs layer (W3) of 38 nm thickness. The line scan reveals that this feature causes an image line with 270 nm full-width half maximum (FWHM). This is again the lateral resolution value that we have obtained above. This example demonstrates that features well below the resolution limit can still be made visible provided that the chemical contrast is strong enough.

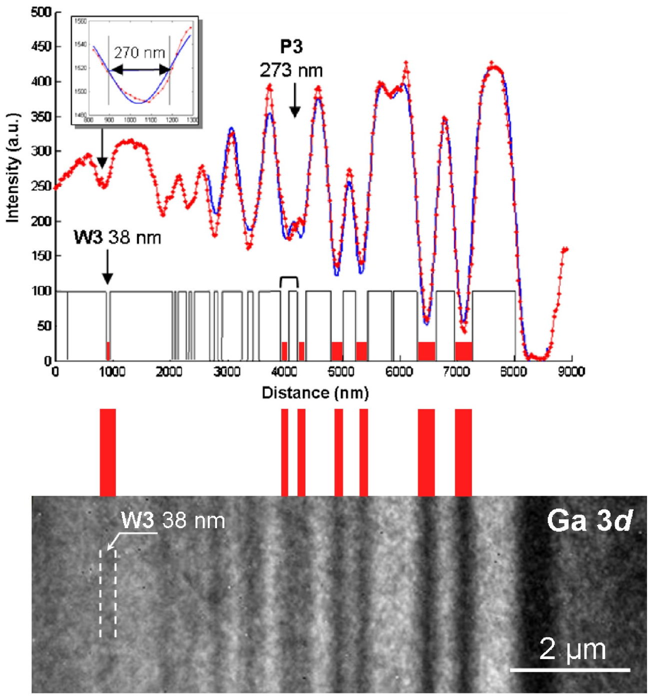

Figure 16: *Energy-filtered image from a GaAs/AlGaAs layered structure acquired at the maximum intensity of the Ga 3d core level peak (kinetic energy of 380.4 eV; incident photon beam of 400 eV). From [37].*

Fermiology – The electron-optical system of a spectromicroscope can be equipped with a transfer lens, by means of which the angular rather than the lateral distribution of the photoelectrons can be projected onto the image detector [38]. This approach permits a very efficient Fermi surface mapping, as an entire two-dimensional slice in reciprocal space can be recorded in a single measurement.

An example for such an experiment from an Ag(111) surface is given in Fig. 17. The picture represents a momentum map of the photoelectrons at the Fermi energy excited with photons of $h\nu = 40.8\,\mathrm{eV}$. It reveals the almost spherical Fermi surfaces in the first (center), 2$^{\mathrm{nd}}$ or next

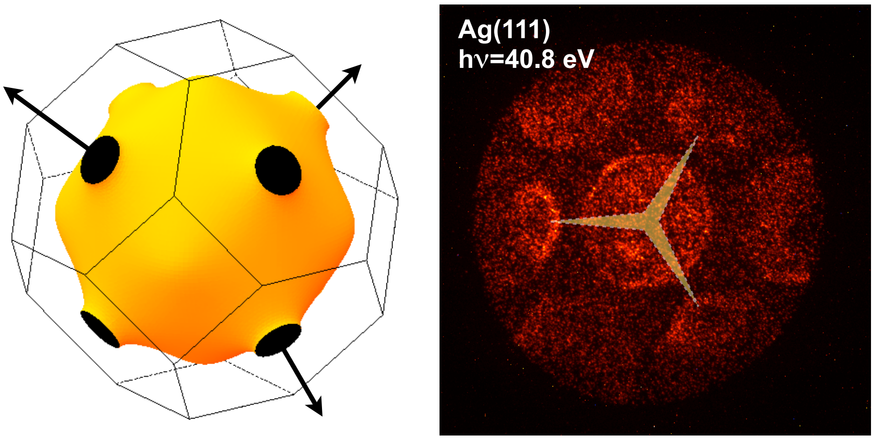

Figure 17: *(Right) Fermi surface mapping of an Ag single crystal along the [111] direction with the NanoESCA at* $h\nu = 40.8\,\mathrm{eV}$ *photon energy. The data show the Fermi surfaces in the nearest neighbor (in the direction of the star spokes) and the next nearest neighbor Brillouin zones. (Left) Calculated Fermi surface for Silver.*

neighbor (along the spokes of the star) and even the 3rd or next nearest neigbor Brillouin zone (BZ). The 1st and 2nd BZ are connected through the characteristic necks (schematic drawing in Fig. 17), whereas the 1st and 3rd BZ are separated by a larger gap. The necks, however, do not show up in the experimental momentum map. By switching between the real and reciprocal space imaging mode in the photoemission microscope, it is possible to directly correlate electronic and chemical structures.

4.2 Spin Effects in Photoemission

The electron spin can give rise to very peculiar phenomena in photoemission experiments. This is due to the fact that the electronic states are subject to two spin-dependent interactions: (i) spin-orbit coupling, and *(ii)* exchange interaction. Whereas spin-orbit coupling is mainly an atomic property, exchange-interaction is at the heart of the many electron system and is responsible for magnetic phenomena.

4.2.1 Ferromagnetic systems

A ferromagnet is characterized by a finite magnetization $\vec{M}$, i.e. a spontaneous long-range magnetic order below a critical temperature T_C. The magnetization is related to a lifting of the spin-degeneracy of the valence electronic states. As a consequence, the spin-up and spin-down bands are separated in binding energy by the exchange splitting $\Delta E_{exc}(\vec{k}, E)$. A spin-resolved photoemission experiment will therefore be able to directly distinguish between the spin-up and spin-down states, as the spin is preserved during the optical transition.

Fig. 18 gives an example for spin-resolved photoemission from the Fe(001) surface. The intensity spectrum (upper panel, solid line) exhibits a strong peak close to the Fermi level and a weaker spectral feature at around 3 eV binding energy. The sample is magnetized within the surface plane and the spin polarization distribution is measured along the magnetization direction (bottom panel). It reveals some structure in the region between E_F and 2 eV binding energy, and levels off to an almost constant value towards higher binding energies. From the intensity and spin polarization distributions we can calculate the spin-up and spin-down contributions to the photoemission spectrum according to eq. 19. These are represented by the closed and open symbols in the upper panel of Fig. 18. We can easily see that these partial spin spectra differ significantly from each other. In a qualitative picture the features marked by A-D can be related to transitions different initial state bands.

According to the nonrelativistic selection rules (see Appendix), the experimental set-up allows access to initial states of mainly Δ_1 and Δ_5 symmetry. By comparison to band structure calculations, the feature *B* can be ascribed to direct transitions from the $\Delta_5^{\downarrow}$-band lying closely below E_F. The other features appear in the majority spin spectrum: peak *A* is located at a binding energy of $E_B = -0.7 \pm 0.2$ eV and originates from an initial state of $\Delta_1^{\uparrow}$ symmetry, whereas feature C positioned at $E_B = -2.5 \pm 0.2$ eV results from the $\Delta_5^{\uparrow}$-band. Finally, a feature labeled D is located at $E_B = -3.4 \pm 0.2$ eV and originates from the strongly dispersive $\Delta_1^{\downarrow}$ band, which starts at the Γ-point. These findings are in good agreement with previous photoemission studies on Fe(001) as presented, for example, in Ref. [39].

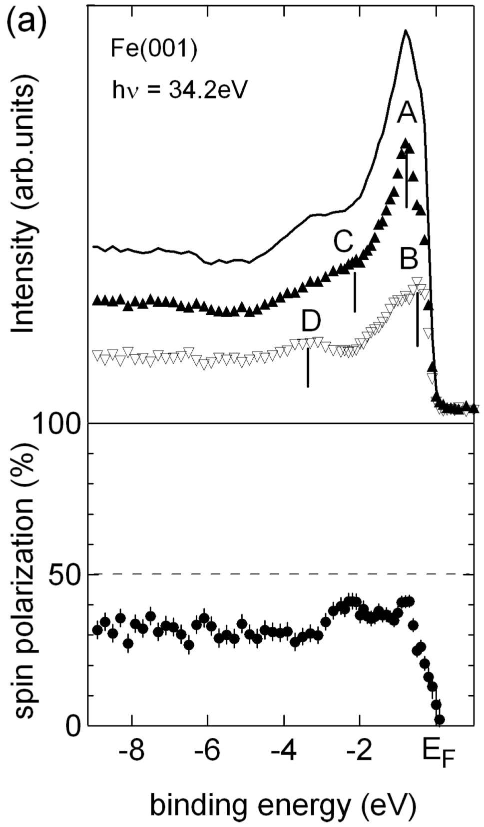

Figure 18: *Top panel: Spin-resolved photoemission spectra from Fe(001) along the surface normal at a photon energy of* $h\nu = 34.2$ *eV for p-polarized light impinging at 45° angle of incidence. The intensity spectrum (solid line) is decomposed into the spin-up (▲) and spin-down (∇) components. These have been extracted on the basis of the spin polarization distribution (bottom panel). The spectral features marked A-D are explained in the text.*

4.2.2 Optical spin orientation

Even in the absence of magnetic interactions, it is possible to observe spin-polarized photoelectrons and relate them to the symmetry of the electronic states. This phenomenon is called “optical spin orientation” and the microscopic mechanism is provided by spin-orbit coupling, as we have already discussed in sect. 2.1.1. The effects are large, if the spin-orbit coupling in the occupied states is strong.

As an example, Fig. 19 shows spin-resolved photoemission data for the W $4f$ shallow core levels obtained with linearly polarized light. The geometry was chosen such that the light impinges on the W(110) surface at a glancing angle of 17°. Symmetry arguments require that the spin-polarization vector is oriented perpendicular to the plane spanned by the direction of incidence an the surface normal [41]. These states show a clear spin-orbit splitting of about $\Delta E_{so} \approx 2.5$ eV between the $4f_{7/2}$ and $4f_{5/2}$. We see that the partial intensity spectra of spin-up (▲) and spin-down (∇) differ significantly at the peak positions, resulting in a positive spin polarization at the $4f_{7/2}$ emission line, whereas the $4f_{5/2}$ level exhibits a negative spin polarization (bottom panel). This spin polarization reversal between the spin-orbit split levels is an instrinsic feature of the optical spin orientation process, because the total spin polarization integrated over all spin-orbit split levels is required to vanish for symmetry reasons – at least in nonmagnetic materials. Note that for a given experimental geometry the sign of the spin polarization is unambiguously connected to the symmetry of the electron states involved in the optical transition. This assertion also holds for band states in a solid and allows a detailed analysis of spin-orbit effects in the band structure on the basis of spin-polarized photoemission experiments [42].

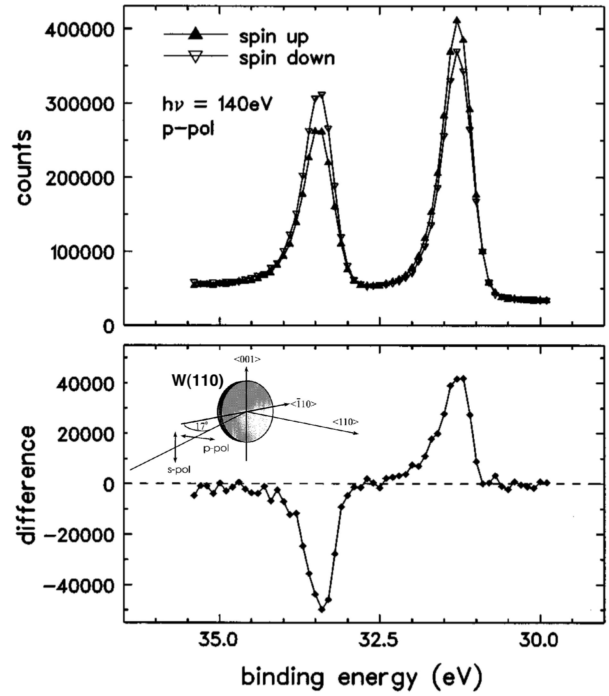

Figure 19: *Spin-resolved W 4f energy distribution curves (EDC's) measured with p-polarized light of hν=140 eV photon energy. The spin polarization vector is oriented perpendicular to the plane spanned by the direction of light incidence and the surface normal. The integral of the difference (lower panel) over the binding energy vanishes within 1% relative to the integral of the absolute value of the difference. From [40].*

4.2.3 Rashba States

The spin-polarization effect described in the previous section is due to the intraatomic spin-orbit interaction in the Hamiltonian (eq. 2). This term has a specific structure. In the field of spin-dependent transport there is a strong desire to control the electron spin in semiconductors by electric fields. In order to describe this situation in a planar configuration, one often uses the Rasbha-Bychkov Hamiltonian [43]. Interestingly, it has a very similar mathematical form

$$H_{RB} = \alpha(-i\vec{\nabla} \times \vec{E}) \cdot \vec{\sigma} \tag{20}$$

with the Rashba constant α and the effective electric field $\vec{E}$. One expects maximal effects of the Rashba Hamiltonian when the electric field, the electron momentum and the electron spin are mutually orthogonal.

In two-dimensional (2D) systems with broken inversion symmetry, this spin–orbit interaction causes spin separation of the moving electrons – which is why it is interesting for spintronics. However, the inversion symmetry of the potential is also naturally broken at any crystal surface or interface. As a consequence, electronic states localized at a surface/interface should be spin-split although this splitting can be quite small. In fact, the Rashba interaction at crystal surfaces becomes sizeable only when it couples to the large intra-atomic spin-orbit interaction. The gradient of the surface potential by itself is not sufficient to cause a directly observable splitting of the surface/interface electronic bands into spin subbands [44]. Therefore, this interaction plays an important role only if high-Z elements are involved at the surfaces or interfaces.

It is well-known that some noble metal surfaces exhibit pronounced surface states. This is also true for the unreconstructed Au(111) surface, which exhibits a Shockley-type surface state at the center of the surface Brillouin zone (SBZ), i.e. at the $\bar{\Gamma}$-point. This situation is depicted in Fig. 20. The surface state is characterized by a parabolic dispersion with $k_{||}$. Due to the Rashba

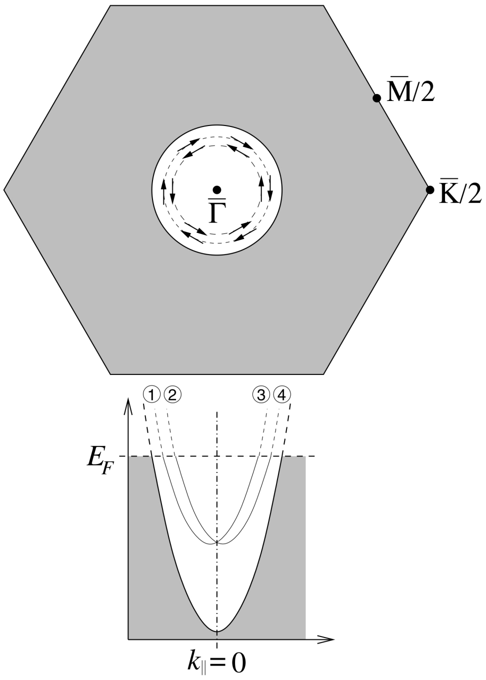

Figure 20: *Upper panel, section of the surface Brillouin zone of the unreconstructed Au(111) surface. The* $\overline{\Gamma K}$ *distance is* $\pi\sqrt{32/3a} = 1.45\mathring{A}^{-1}$. *Lower panel, schematic view of the split surface state dispersion in a cut through* $\bar{\Gamma}$. *From [45].*

interaction the surface state will spin-split, forming two concentric ring-shaped Fermi surfaces with opposite spin polarization in the SBZ.

Indeed this splitting can be clearly seen in a high-resolution photoemission experiment, (Fig. 21). The gray-scale intensity map represents a slice through the Brillouin zone along the direction $\bar{\Gamma}\bar{K}$. Without the Rashba interaction there would be only one parabolic trace centered around $k_{||} = 0$, corresponding to the dispersion of the surface state. The Rashba interaction introduces a symmetric splitting resulting in two parabolic traces with opposite spin polarization. The energy and momentum distribution curves show that the two traces are only degenerate at $k_{||} = 0$, but separated otherwise.

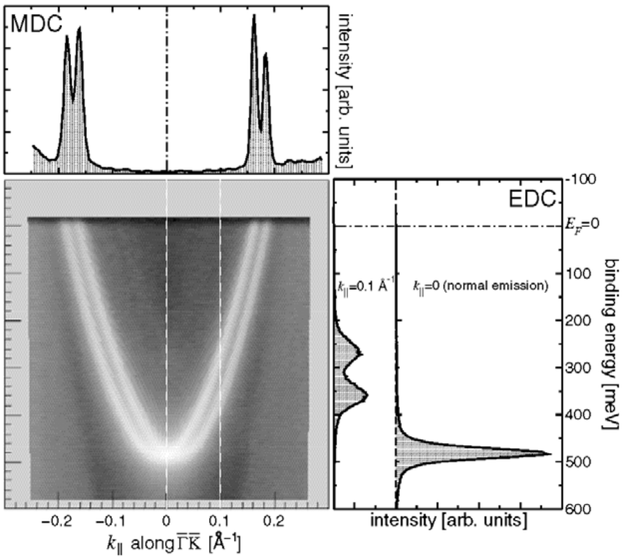

Figure 21: *Photoemission intensity of the Shockley state on Au(111) as a function of energy and momentum* $I(E_B, k_{||})$ *(white means high intensity). The top panel shows a cut at constant energy* $E = E_F$ *(MDC); the right-hand panel gives the energy distribution curves (EDCs) at* $k_{||} = 0$ *and* $k_{||} = 0.1\,\mathring{A}^{-1}$. *From [45].*

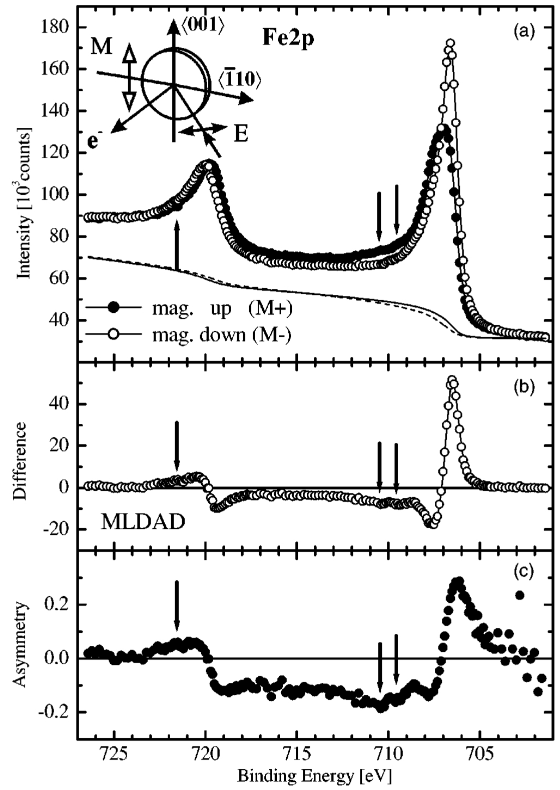

Figure 22: *(a) Fe 2p photoemission spectra and Shirley background of 15 ML Fe / W(110) excited with p-polarized radiation ($h\nu$ =850 eV) for magnetization up and down (M+, M−). The inset shows the experimental geometry. (b) The intensity difference (MLDAD) of the curves from (a). (c) MLDAD asymmetry (without background). The arrows mark the position of correlation-induced satellites. From [47].*

The (111) surfaces of silver and copper have very similar Shockley surface states, but a Rashba splitting could not be confirmed yet. This may be due to the smaller intraatomic spin-orbit coupling as mentioned above.

4.2.4 Magnetic Dichroism in Photoemission

What happens, if we have an experimental situation as described in sect. 4.2.2, but our sample is actually ferromagnetic? Let us take the example of a $2p$ core level. The ferromagnetic state is responsible for a spin-dependent energy splitting of the electronic states – not only in the valence states, but also in the core levels. These split according to their magnetic quantum number m_J, i.e. the $2p_{3/2}$ level splits into 4 sublevels ($m_{3/2}$, $m_{1/2}$, $m_{-1/2}$, $m_{-3/2}$), the $2p_{1/2}$ into two. The transition matrix elements depend on m_J *and* the orientation of the magnetization. As a consequence, the fine structure of the intensity spectrum depends on the magnetization direction. This phenomenon is called magnetic dichroism and is observed for both core levels and valence states [46].

This effect is shown in Fig. 22 for the $2p$ core level photoemission from Fe. Note that we have a very similar geometry as in experiment described in sect. 4.2.2. The magnetization vector is oriented perpendicular to the reaction plane. The upper panel compiles the photoemission spectra across the spin-orbit split $2p$ levels. We can clearly see that the spectra differ significantly for opposite magnetization directions. The difference of the two spectra is plotted in the center panel and reveals characteristic bipolar signatures at the position of the core levels. We also note that the polarity of these features reverses between the $2p_{3/2}$ and the $2p_{1/2}$. This is consistent with the spin polarization change in the optical spin orientation experiment in sect. 4.2.2. In fact, as a general rule, optical spin orientation phenomena in nonmagnetic materials

are taking the form of magnetic dichroisms in ferromagnets.
The magnetic dichroism signal is often expressed as an intensity asymmetry A

$$A = \frac{I(M+) - I(M-)}{I(M+) + I(M-)}. \tag{21}$$

which reveals a similar spectral dependence than the difference. Additional weak spectral features are related to correlation effects (see Sect. 4.3). As the experiment has been performed with linearly polarized light, the effect is also termed magnetic linear dichroism in the photoelectron angular distribution (MLDAD). The latter points out that the size and sign of the magnetic dichroism depends strongly on the emission angle of the photoelectrons analyzed. A closer theoretical analysis shows, that the MLDAD is actually an interference effect between the two photoemission channels into s and d final states [48].

4.3 Electronic Correlations

It is well established nowadays that photoemission spectra of narrow-band materials, such as the elements of the d transition-metal series and their compounds, cannot be entirely explained within a one-electron picture. This is due to the presence of local correlations between electrons in the partially filled d band. Experimental band mapping and its comparison with theoretical results can be a powerful tool to directly investigate correlation effects. It has to be realized, however, that the correlated electron picture is less transparent than the single particle model. The interactions due to the electronic correlations lead to a "dressing" of the single particle, i.e. when the particle moves in the solid it is always screened by these many-particle interactions. This system of particle and interaction cloud may be seen as a new quasiparticle. The respective many-electron calculations result in quasiparticle spectral functions rather than conventional band structures, which is a significant conceptual difference.
From all d transition metals, Ni has the narrowest bands and exhibits the strongest correlation effects. This can be seen in Fig. 23. Panel (a) reproduces a set of experimental angle-resolved

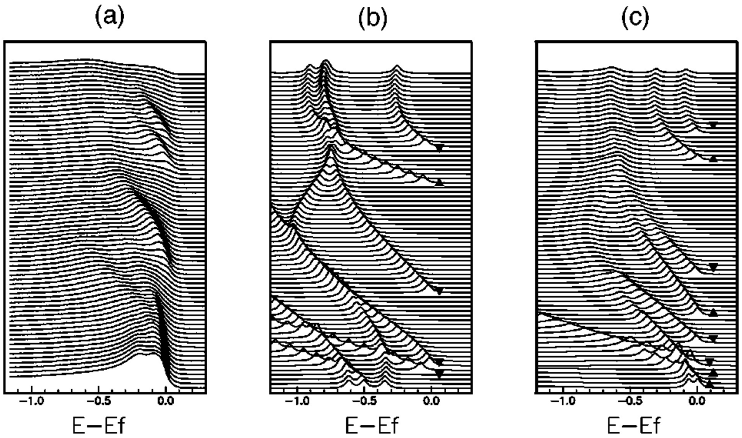

Figure 23: *Comparison between angle-resolved photoemission spectra from a Ni(110) surface at* $h\nu = 21.2\,\mathrm{eV}$ *(a), single particle local-density approximation (LDA) (b), and quasiparticle calculations results (c). The polar angle ranges from 0° (bottom) to 70° (top). The spin character is indicated by ▲ and ▼. From [49].*

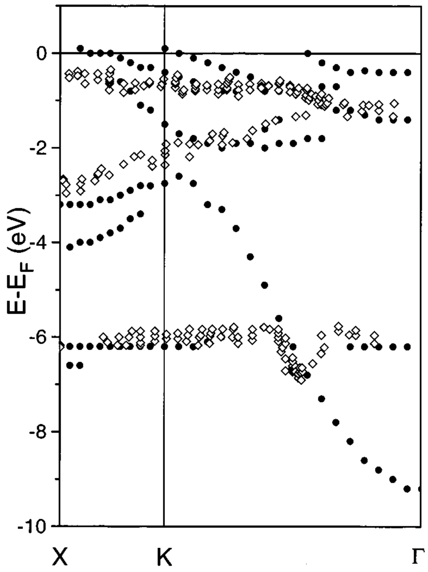

Figure 24: *Comparison between the calculated dispersion of quasiparticle states (●) for majority-spin bands and angle- resolved spin-integrated photoemission results (◊) of Ref. [51]. From [52].*

photoemission spectra, which have been recorded for different emission angles from normal emission up to 70°. It is obvious that the spectral features disperse with the emission angle. A comparison with a single particle particle calculation in the LDA approximation (panel b), however, predicts a much stronger dispersion of the bands than observed in the the experiment. In particular, strong spectral features should also be expected at binding energies larger than 0.5 eV. This is also not observed in the experiment. Furthermore, the exchange splitting between bands of the same symmetry is calculated about twice as large, as observed in spin-resolved experiments ($\Delta E_{exc} \simeq 300\,\mathrm{meV}$ [50]).

The quasiparticle spectral functions calculated within a multiorbital Hubbard model for the experimental geometries are compiled in panel (c) of Fig. 23. The inclusion of correlation effects strongly modifies the spectra: all the structures are pushed up towards E_F by self-energy corrections reproducing much more closely the experimental results both in terms of energy position and dispersion. The spin dependence of the self-energy, arising from the different efficiencies of the scattering channels involving majority- and minority-spin electrons, strongly affects the spin polarization of the quasiparticle states. For this particular region in k space, four spin-up and four spin-down bands are theoretically predicted in the energy region of interest. While in the single-particle picture one spin-up band and four spin-down bands cross the Fermi energy, all four spin-up bands come close to E_F after the inclusion of correlation effects. Moreover, the energy separation between the spin-up and spin-down bands between $\theta = 50°$ and $60°$ is reduced by self-energy corrections. All this is in excellent agreement with the experimental data.

In addition to a spin- and energy dependent renormalization of the quasiparticle states due to the self energy, the correlations also lead to the appearance of new spectral features, which are completely absent in the single particle band structures. The most prominent feature in Ni is the famous “6 eV satellite”. This is depicted in Fig. 24, which shows the calculated dispersion of the majority spin quasiparticle states. These are compared to spin-integrated, angle-resolved photoemission results. In the region close to E_F we observe the spin-dependent energy renormalization already discussed above. In addition, we find a strong dispersing feature corresponding to the sp-type band. At about 6 eV below the Fermi level, however, there appears a new non-dispersing feature. This is the correlation-induced satellite, which indeed turns out to be of majority-spin character in spin-resolved photoemission experiments [53].

4.4 Kinkology

The on-site Coulomb interactions leading to the correlation phenomena discussed above are relatively strong and thus lead to large effects in the band structure. High-resolution photoemission nowadays provides the opportunity to study also the influence of much weaker interactions affecting the electronic system, for example, electron-phonon or electron-magnon interactions. As the analysis procedure is connected close to finding and identifying kinks and precisely measuring the spectral width in the dispersion of the quasiparticle states, this field is sometimes coined “kinkology”.

4.4.1 Electron-phonon interaction

The interaction of different quasiparticles, such as electrons and phonons, results in a crossing and hybridization of their respective dispersion relations. At the position in k-space where such crossings occur, the states involved are shifted in energy with respect to the noninteracting case. As phonons have very low energies of the order of 100 meV the respective modifications of the dispersion behavior of the electronic quasiparticle states due to the electron-phonon interaction will be confined to a narrow region below the Fermi level. Formally, the electron-phonon interaction can be considered as an additional contribution to the self energy Σ.

All characteristics of the electron-phonon coupling (EPC) are described by the *Eliashberg function* $E(\omega, \varepsilon, \vec{k}) = \alpha^2(\omega, \vec{k})F(\omega, \varepsilon, \vec{k})$, the total transition probability of a quasi-particle from/to the state $(\varepsilon, \vec{k})$ by coupling to phonon modes of frequency ω [54]. Information about the Eliashberg function can be obtained from the angle-resolved photoemission spectra, both through the EPC distortion of the quasi-particle bands near the Fermi energy and the temperature-dependent linewidth. If $\varepsilon_0(\vec{k})$ is the bare quasi-particle dispersion of a surface state without EPC, then the measured dispersion $\varepsilon(\vec{k})$ with electron-phonen coupling is given by

$$\varepsilon(\vec{k}) = \varepsilon_0(\vec{k}) + \mathrm{Re}\Sigma(\vec{k}, \varepsilon) \tag{22}$$

The screening of the electrons by the lattice is represented by the self-energy function $\Sigma(\vec{k}, \varepsilon)$. The imaginary part of the self-energy is related to the EPC contribution to the lifetime τ of the excited electronic states,

$$1/\tau = 2\mathrm{Im}\Sigma(\vec{k}, \varepsilon, T) \tag{23}$$

Based on these considerations the influence of the electron-phonon coupling has been investigated in Be($10\bar{1}0$) [55]. The photoemission data in Fig. 25 (left) show the dispersion of the surface states S1 and S2 as bright features. The experimental dispersion of the quasiparticle band $\varepsilon(\vec{k})$ (Fig. 25, right) is compared to the expected dispersion of the surface state without additional interactions $\varepsilon_0(\vec{k})$. This comparison reveals a weak, but distinct deviation of the experimental data from the parabolic dispersion close to the Fermi energy. This kink is the spectral signature of the electron-phonon coupling.

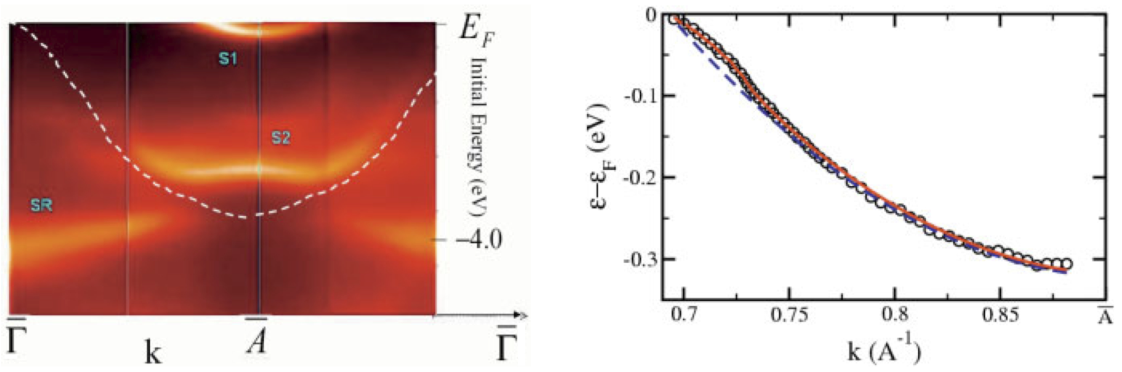

Figure 25: *(Left panel) Energy vs. momentum photoemission display of the two surface state bands S1 and S2 on Be*($10\bar{1}0$)*. The dashed line is the bulk band edge. Data taken at 30 K at 40 eV photon energy. (Right panel) Quasi-particle dispersion determined from momentum distribution curves (circles) obtained at 24 eV photon energy. Dashed blue line is the bare particle dispersion* $\varepsilon_0(k)$ *and the red line is the fit to the data from the extracted Eliashberg function. From [55].*

4.4.2 Electron-magnon interaction

In a magnet we have collective excitations of the spin system – magnons. These quasiparticles have energies also in the 100 meV range. We should therefore expect that electron-magnon interaction leads to the appearance of kinks in the band structure of ferromagnetic materials. This is demonstrated for the photoemission from the Fe(110) surface. The ARPES data (Fig. 26) show the spectral distribution of the surface state photoemission close to E_F at the center of the surface Brillouin zone. A careful analysis of surface state dispersion reveals a characteristic

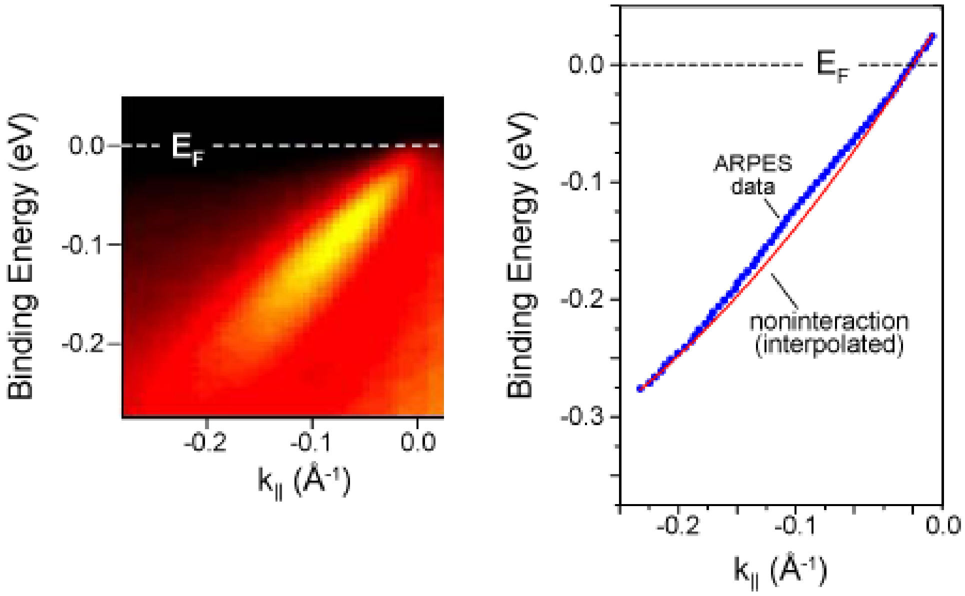

Figure 26: *ARPES data from the iron (110) surface state. Left: Raw data, showing the intense quasiparticle region. Right: The electron band dispersion (*E *vs.* $k_{||}$ *) extracted from the data reveals a weak "kink" in the region between 0.1 and 0.2 eV below* E_F*. From [29].*

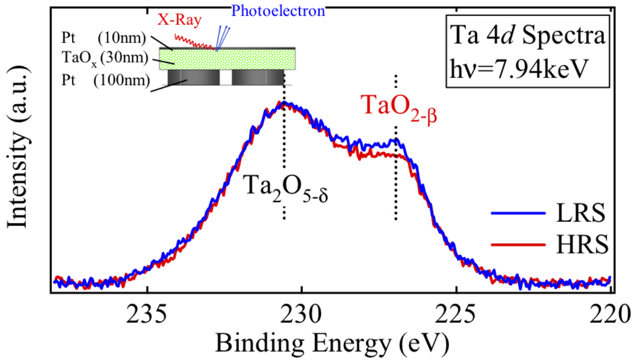

Figure 27: *Hard x-ray photoemission spectra from Ta_2O_5 in the high (HRS) and low resistive state (LRS). From [58].*

deviation from the parabolic behavior in the regime down to 200 meV below the Fermi level. This broader kink structure can be indeed related to the electron-magnon interaction [29]. From these data it is possible to extract the strength and extension of the electron magnon interaction.

4.5 High-Energy Photoemission (HAXPES)

So far we have discussed effects in valence band and core level photoelectron spectroscopy at excitation energies below 1000 eV. As we know from the inelastic mean free path curves under these conditions we will have $\lambda_{in} \simeq 1\mathrm{nm}$ at best, i.e. all of these experiments are more or less surface sensitive. In recent years there is a strong effort to extend photoelectron spectroscopy also to higher excitation energies up to 10 keV in order to overcome this limitation. The approach is coined HArd X-ray PhotoElectron Spectroscopy (HAXPES) and poses several experimental challenges [56]. First, the electron spectrometers must be modified to be able to measure photoelectrons with high kinetic energy and good energy resolution ($\Delta E < 100\,\mathrm{meV}$). Second, the photoexcitation cross section for most core levels drops by 2-3 orders of magnitude, when going from 1 keV to 10 keV photon energy. As a consequence, the resulting photoelectron intensity will be small and difficult to measure. This can be only partially compensated on the primary side, i.e. by increasing the photon flux. At present, HAXPES experiments are still demanding and very difficult to carry out with laboratory sources. With synchrotron radiation, however, HAXPES is quickly maturing into a powerful tool for materials characterization.

Laterally Integrating Spectroscopy – The major advantage of HAXPES is its larger information depth which permits the access to buried layers and interfaces. The example shown in Fig. 27 is taken from the field of resistive oxides. Usually, oxides are wide band gap insulators. As is discussed in Chapter E4, some of these materials may change their conductivity by several orders of magnitude, if a short current pulse above a certain threshold is applied to the material [57]. This current leads to the formation of conductive filaments or a local valency change in the oxide generating carriers for electrical transport. This is called the low resitive state (LRS). Interestingly, this process is reversible and the system may also be switched back into the high resistive state (HRS). This behaviour considered as a future memory principle and explains the strong interest in resistive oxides.
Ta_2O_5 is one of the promising materials that is currently thoroughly investigated with respect to resistive memory applications. Fig. 27 shows the comparison of photospectra taken from the Ta $4d$ core states with about 8 keV photon energy. In order to switch the conductivity of the Ta_2O_5 film a bottom and top electrode usually made from Pt is needed, through which the switching

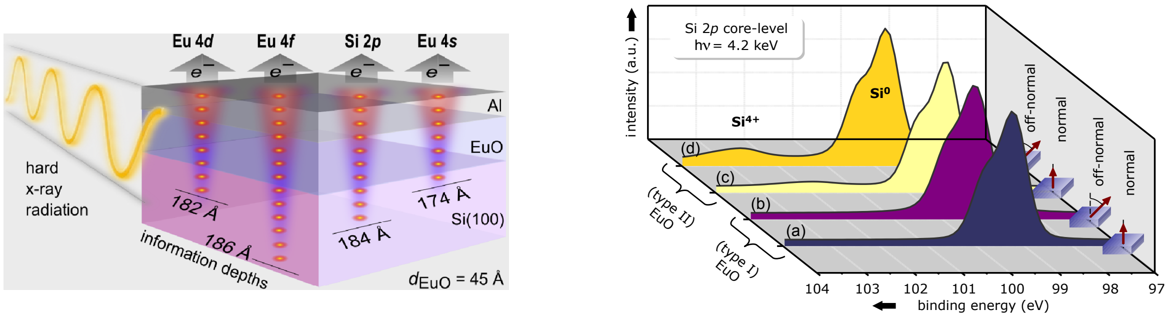

Figure 28: *HAXPES on the EuO/Si interface. (Left) Schematic representation of the information depth for the different Eu and Si core levels. (Right) Si 2p core level photoemission spectra for (type I) stoichiometric EuO and (type II) O-rich EuO, recorded at 4.2 keV photon energy in normal (0°) and off-normal (60°) electron emission geometry. From [61].*

current is passed through the insulator. This means, however, that the photoemission experiment has to probe the region below the Pt electrode, which requires a sufficiently high information depth. As can be seen, the experiment is indeed able to find a difference in the relative core level intensities underneath the 10 nm thick Pt-electrode, which can be related to a change of the oxidation state from Ta^{5+} to Ta^{4+} between the HRS and LRS state [58]. This demonstrates that HAXPES is able – at least in principle – to follow and map the valency changes taking place during the resistive switching process.

The second example relates to the field of spintronics. Magnetic tunneling barriers are considered as a means to enable an efficient spin injection into semiconductors [59, 60]. One of the materials for spin-filter barriers investigated in this context is the ferromagnetic semiconductor EuO. In order to obtain a well-defined system for spin injection, a chemically and structurally sharp interface between EuO and the semiconductor – preferably Silicon – must be established during the growth process. Of particular importance is the control of the oxygen partial pressure, as excess oxygen leads to a formation of interfacial silicon oxide.

The chemical quality of the EuO/Si interface can be addressed by HAXPES exploiting the kinetic energy dependence of the photoelectron inelastic mean free path (Fig. 28) [61]. The thickness of the EuO film ($d_{EuO} = 45$ Å) has been chosen such that for a given photon energy (4.2 keV) the photoelectrons from the Si 2p levels reaching the spectrometer originate mainly from the interfacial region between EuO and Si. The interface sensitivity can be even increased by changing the take-off angle of the electrons from normal emission to off-normal emission. As can be seen in Fig. 28 the growth of "oxygen-rich" EuO (type II) leads to a significant photoemission satellite in the Si 2p spectrum which stems from a Si^{4+}state. The spectral weight of this contribution increases for the off-normal emission geometry. This is a clear indication that the silicon oxide contribution is located at the EuO/Si interface. The growth of "stoichiometric" EuO takes place at a lower oxygen partial pressure. The respective Si 2p spectra prove the absence of an oxide component, i.e. the interface between EuO and Si is chemically sharp. The results for the Eu 4d, 4f, and 4s core level photoemission corroborate the findings.

Recent experiments have demonstrated that high-energy photoemission can also be used to carry out bulk-sensitive band mapping experiments [62–65].

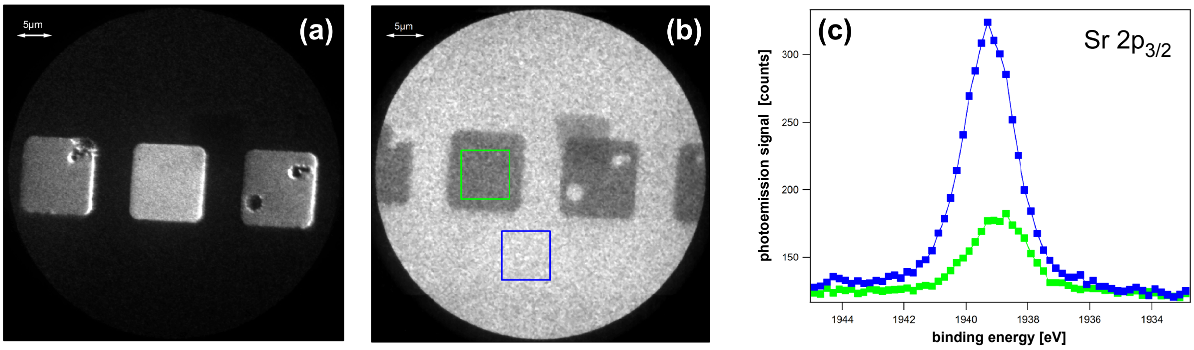

Figure 29: *Laterally resolved HAXPES on Au microstructures on $SrTiO_3$. (a) threshold photoemission, (b) Sr $2p_{3/2}$ photoelectron distribution at $h\nu = 6500$ eV, and (c) local photoelectron spectra from the regions of interest (blue, green).*

High-Energy Spectromicroscopy – The NanoESCA system offers a possibility to perform HAXPES experiments with lateral resolution. A first demonstration for a resisitive material is given in Fig. 29. The sample consists of 10 nm thick Au electrode micropatterns on a $SrTiO_3$ substrate, which show up as bright areas in threshold photoemission. At a photon energy of $h\nu = 6500$ eV, the kinetic energy of the $2p_{3/2}$ photoelectrons is high enough to allow them to penetrate the Au electrode. The respective photoelectron distribution recorded with the NanoESCA exhibits a weaker photoemission signal from the area of the electrodes (Fig. 29b) than from the uncovered part of the $SrTiO_3$ substrate. The lateral resolution in this experiment is about 500 nm. In order to obtain photoemission spectra, a sequence of images at different kinetic energies covering the photoemission peak has been acquired. This image stack is analyzed by integrating the intensity in each image for the two marked regions of interest (blue and green) and plotting it as a function of the kinetic energy. This analysis yields the local $2p_{3/2}$ photoemission spectra in Fig. 29c. The relative difference in the total intensities of the two spectra relates to the damping by the Au layer. One also notes, however, a slight shift of the peak position between the two spectra. This suggests that the chemical states of the covered and uncovered surface areas are slightly different. This experiment demonstrates that HAXPES can also performed with sub-micrometer lateral resolution.

4.6 Interfacial sensitivity

In Sect. 4.5 we have demonstrated two ways to vary the surface sensitivity in photoemission: changing the photon energy so as to move along curves of the type in Figure 5 and varying the take-off angle, as indicated e.g. in Figure 28. Both of these involve electron escape processes. One may also ask if there is a way to somehow tailor the photon wave field so as to vary surface sensitivity. Creating an x-ray standing wave is one method for doing this, and it has been found possible to selectively look at buried layers and interfaces [66], as well as element-resolved densities of states [67], in this way.

In Figure 30, we illustrate one approach for using soft x-ray (or in the future also hard x-ray) standing waves to carry out more precise depth-resolved photoemission from multilayer nanostructures [66]. This x-ray standing wave (XSW) approach combines a standing wave created by first-order Bragg reflection from a multilayer mirror of period d_{ML} with a sample in which one layer has a wedge profile, and can be termed the “swedge method”. If the standing

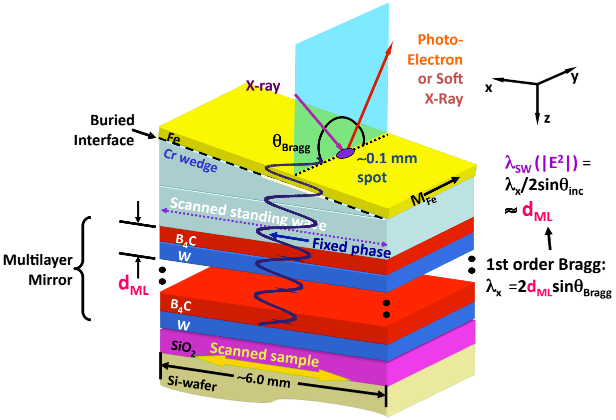

Figure 30: *Schematic illustration of the simultaneous use of an x-ray standing wave plus a wedge-profile overlayer sample to selectively study buried interfaces and layers – the "swedge" method. In the example here, a strong standing wave (SW) is created by first-order Bragg reflection from a multilayer made of repeated B_4C/W bilayers, and a Cr wedge underneath an Fe overlayer permits scanning the SW through the Fe/Cr interface by scanning the sample along the x direction. From ref. [66].*

wave is created by a typically well-focussed synchrotron radiation beam, then its dimensions will be much smaller than a typical sample, as indicated in the figure. Since the standing wave only exists in the region where the beam hits the sample surface, and its phase is locked tightly to the multilayer mirror, scanning the sample in the photon beam along the x direction effectively translates the standing wave through the sample. In the example shown, the standing wave would in particular scan through the Fe/Cr interface of interest, at some positions being more sensitive to the Fe side and at some more sensitive to the Cr side.

Some results obtained with this method for the Fe/Cr interface are summarized in Figs. 31 and 32. The analysis combined XPS intensity and MCDAD measurements (not shown here) from the 3p and 2p core levels of Fe and Cr, respectively. In Figure 31a is shown the variation of the Cr3p/Fe3p ratio as the sample is scanned in the way suggested above, for several angles of incidence near the Bragg angle. Oscillations in this ratio clearly reflect the passage of the standing wave node and belly through the interface. In Figure 31b we compile "rocking curves" in which the angle is varied around the Bragg angle for different positions x along the sample, or equivalently different Cr wedge thickness d_{Cr}. There are dramatic changes in the intensity ratio in this data also.

Self-consistently analyzing these data with x-ray optical calculations of standing-wave photoemission and only two variable parameters (the depth of onset of change in the Fe composition and the width of a linear gradient as the interface changes from pure Fe to pure Cr) yields the excellent fits shown to both types of data, and the parameters given at the left side of Figure 32a. The MCDAD data for both Fe 2p and Cr 2p core level photoemission have also been measured as the sample is scanned in the beam. The relative signs of the MCDAD signal for the Fe 2p and Cr 2p levels are found to be opposite [66]. this immediately implies that a small amount of Cr is oppositely magnetized compared to Fe, and this must be induced by the ferromagnetic Fe layer, since Cr is normally antiferromagnetic. Similar data have been obtained at the 3p levels of Cr and Fe. Further analyzing this data set with two parameters for Fe 2p and 3p MCD and two parameters for Cr 2p and 3p MCD yields the atom-specific magnetization profiles shown at right hand side of Figure 32a.

Thus, in the above described experiment the swedge method has permitted non-destructively determining the concentration profile through an interface, as well as the atom-specific magnetization contributions through it. The swedge approach has also been used successfully to determine layer-specific densities of states that can be linked changes in magnetoresistance as a function of nanolayer thicknesses [68]. Several other possible applications of it have also been

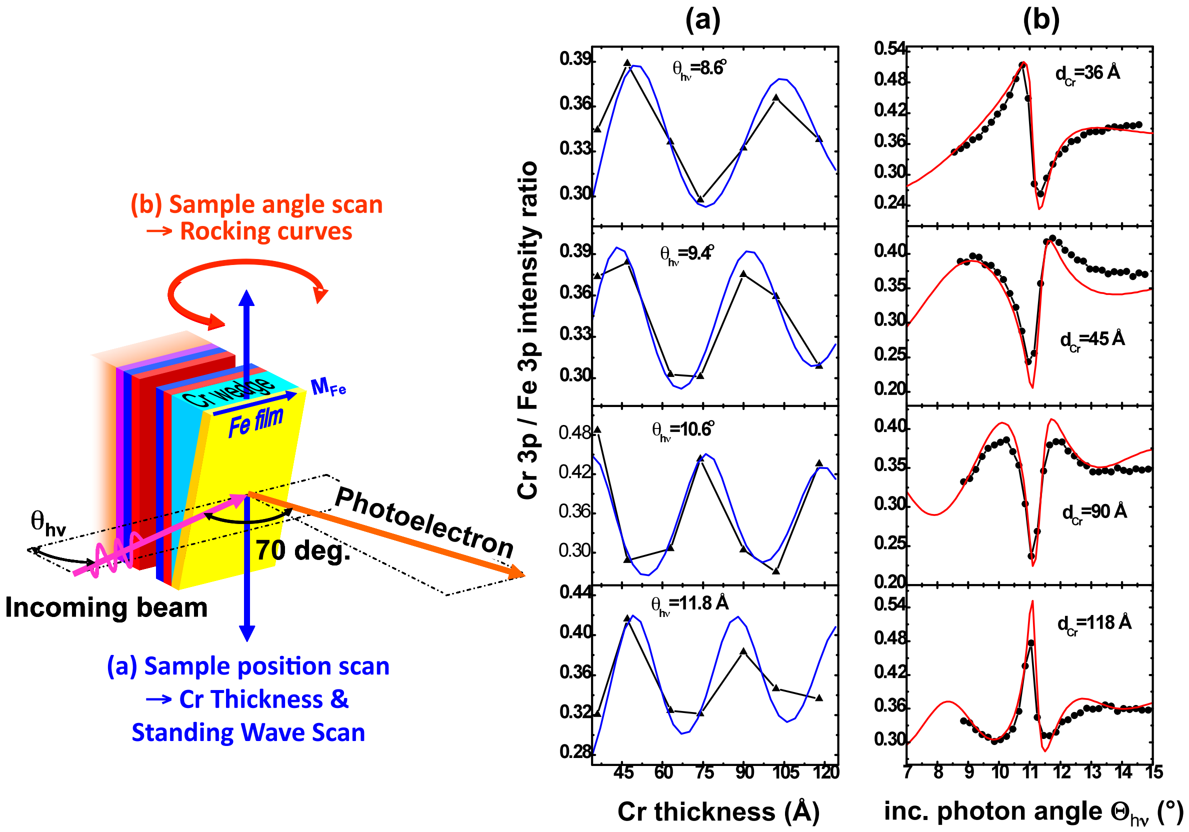

Figure 31: *Experimental and calculated Cr3p/Fe3p ratios for two types of standing wave scan for the sample shown in Figure 21: (a) Scanning the sample along x at fixed incidence angle, as indicated in Figure 30, and (b) scanning the sample polar angle with fixed x position (or Cr thickness). The best-fit theory curves are for the parameters shown at the left of Figure 24(a). From ref. [66].*

suggested [66,69,70], including going to hard x-ray excitation, for which reflectivities and thus standing wave strengths can be much higher.

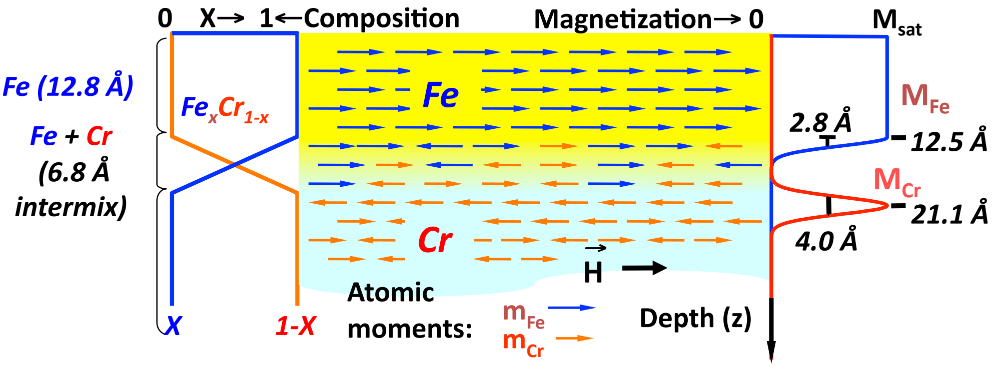

Figure 32: *The concentration and atom-specific magnetization profiles through the Fe/Cr interface, as derived from the XPS and MCDAD experiments. From ref. [66].*

5 Conclusions

In this contribution, we could only touch upon selected aspects of photoelectron spectroscopy and photoemission processes. It should have become clear that this spectroscopy with its many facets provides a powerful tool for an *en detail* electronic and chemical characterization of materials. Very important information can already be extracted by means of qualitative interpretation schemes. The full potential, however, can be unleashed by quantitative descriptions within sophisticated photoemission calculations. The successful expansion of photoemission techniques to hard x-ray excitation relaxes the constraint of surface sensitivity. HAXPES offers access to genuine bulk electronic structures and buried interfaces.

Acknowledgement

The author is indepted to the Jülich spectroscopy and microspectroscopy groups at the storage ring facilities DELTA (Dortmund), BESSY (Berlin) and ELETTRA (Trieste), particularly S. Cramm, S. Döring, V. Feyer, D. Gottlob, A. Herdt, I. Krug, F. Nickel, M. Patt, L. Plucinski, and C. Wiemann.

Sincere thanks are due to C. S. Fadley (ALS Berkeley), A. X. Gray (SLAC), A. M. Kaiser (SPECS GmbH), M. Merkel (Focus GmbH), and M. Escher (Focus GmbH) for ongoing collaboration and the permission to use material for this lecture.

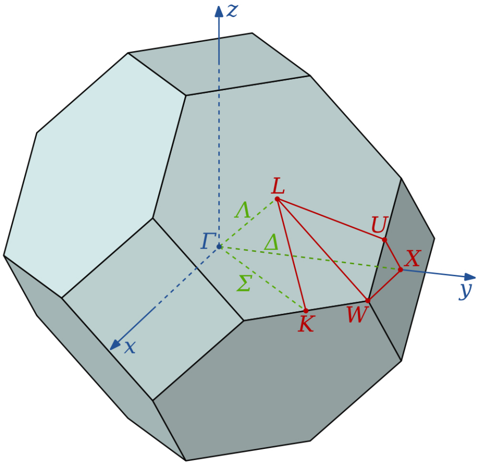

Figure 33: *Brillouin zone of an face-centered cubic crystal with high-symmetry directions (green) and high-symmetry points (red).*

Appendix I : Optical Selection Rules

The strength of the optical interband transitions in the electronic structure of a solid is determined by dipole selection rules. These dipole selection rules depend on the symmetry of the crystal and the experiment and have been derived from group-theoretical arguments. In the following, we will give an example for the dipole selection rules valid in a face-centered cubic crystal.

The symmetry of the electronic wavefunctions in the initial and final state of the photoemission process is described by so-called irreducible representations A_i of the symmetry group. The letter A usually refers to high-symmetry directions and points in the Brillouin zone (Fig. 33). Depending on the structure of the Hamiltonian (see, for example, eq. 2) one may distinguish *nonrelativistic* or *single-group representations* (spatial symmetry only), *relativistic* or *double-group representations* (including spin-orbit coupling) and *magnetic co-representations* (spin-orbit coupling and exchange interaction). The dipole operator of the photon field can also be expressed by an appropriate representation, taking into account the experimental geometry (direction of light incidence). For an fcc crystal, we have the following representations without and with spin-orbit coupling along the three high-symmetry directions

crystalline axis	symmetry label	nonrelativistic	relativistic
{001}	Δ	Δ_1, Δ_2,$\Delta_{2'}$,Δ_5	$\Delta_6^1, \Delta_6^5, \Delta_7^2, \Delta_7^{2'}, \Delta_7^5$
{011}	Σ	$\Sigma_1, \Sigma_2, \Sigma_3, \Sigma_4$	$\Sigma_5^1, \Sigma_5^2, \Sigma_5^3, \Sigma_5^4$
{111}	Λ	Λ_1, Λ_3	$\Lambda_{4,5}^3, \Lambda_6^1, \Lambda_6^3$

Table 1:

Electronic states with the highest symmetry have the lowest number, i.e. $\Delta_1, \Sigma_1, \Lambda_1$. In a photoemission process along the surface normal of a low-index surface, the electron is excited into a final state with the highest symmetry inside the crystal, which connects to a spherical wave (corresponding to a s wavefunction) outside the crystal propagating towards the detector. For this normal emission geometry, we have the following dipole selection rules between single-group representations [71]

In the presence of spin-orbit coupling, the interband transitions take place between double-group representations and lead to the excitation of spin-polarized photoemission due to the

	final state			
initial state	Δ_1	Δ_2	$\Delta_{2'}$	Δ_5
Δ_1	$\parallel$			$\perp$
Δ_2		$\parallel$		$\perp$
$\Delta_{2'}$			$\parallel$	$\perp$
Δ_5	$\perp$	$\perp$	$\perp$	$\perp$

	final state			
initial state	Σ_1	Σ_2	Σ_3	Σ_4
Σ_1	$\parallel$		X	Y
Σ_2		$\parallel$	Y	X
Σ_3	X	Y	$\parallel$	
Σ_4	Y	X		$\parallel$

	final state	
initial state	Λ_1	Λ_3
Λ_1	$\parallel$	$\perp$
Λ_3	$\perp$	$\parallel,\perp$

Table 2: *$\vec{A}$ parallel ($\parallel$) and perpendicular ($\perp$) to the surface normal, and parallel to the x-axis (X) or y-axis (Y), respectively.*

mechanism of optical spin-orientation. An example for the resulting relativistic selection rules with circularly polarized light are given in Table 3. For a full set of relativistic selection rules, the reader is referred to Ref. [72].

	final state				
initial state	Δ_6^1	Δ_7^2	$\Delta_7^{2'}$	Δ_6^5	Δ_7^5
Δ_6^1				$\vert\Uparrow\rangle$	$\vert\Downarrow\rangle$
Δ_7^2				$\vert\Downarrow\rangle$	$\vert\Uparrow\rangle$
$\Delta_7^{2'}$				$\vert\Downarrow\rangle$	$\vert\Uparrow\rangle$
Δ_6^5	$\vert\Downarrow\rangle$	$\vert\Uparrow\rangle$	$\vert\Uparrow\rangle$		
Δ_7^5	$\vert\Uparrow\rangle$	$\vert\Downarrow\rangle$	$\vert\Downarrow\rangle$		

Table 3: *Relativistic dipole selection rules for normal emission along the Δ line and excitation with right-hand circularly polarized light. The spin-polarization is oriented along the surface normal (z-axis) and can be positive ($\vert\Uparrow\rangle$) or negative ($\vert\Downarrow\rangle$). For excitation with left-hand circularly polarized light, $\vert\Uparrow\rangle$ and $\vert\Downarrow\rangle$ have to be interchanged.*

References

[1] S. Hüfner, *Photoelectron Spectroscopy* 3rd ed. (Springer, Berlin, 2003).

[2] *Solid-State Photoemission and Related Methods*, eds. W. Schattke, and M. A. van Hove (Wiley-VCH, Weinheim, 2003).

[3] F. Reinert and S. Hüfner, New J. Phys. **7**, 97 (2005).

[4] *Very High Resolution Photoelectron Spectroscopy*, ed. S. Hüfner (Springer, Berlin, 2007).

[5] F. de Groot and A. Kotani, *Core Level Spectroscopy of Solids* (CRC Press, Boca Raton, 2008).

[6] R. A. Millikan, Phys. Rev. **7**, 355 (1916).

[7] H. Hertz, Annal. Phys. **267**, 983 (1887).

[8] A. Einstein, Annal. Phys. **322**, 132 (1905).

[9] C. Nordling, E. Sokolowski, and K. Siegbahn, Phys. Rev. **105**, 1676 (1957).

[10] *Handbook on Synchrotron Radiation* Vol. 1A, B, edited by D. Eastman and Y. Farge (North-Holland Publishing, Amsterdam, 1983).

[11] M. Salmeron and R. Schlögl (2008). Lawrence Berkeley National Laboratory Paper LBNL-183E. Retrieved from: http://www.escholarship.org/uc/item/6n75v256.

[12] R. M. Martin, *Electronic Structure – Basic Theory and Practical Methods* (Cambridge University Press, Cambridge, 2004).

[13] K. Horn, in *Handbook of Surface Science*; Vol. 2, edited by K. Horn and M. Scheffler (Elsevier, Amsterdam, 2000), p. 383.

[14] *Optical Orientation*, edited by F. Meier and B. P. Zakharchenya (North-Holland, Amsterdam, 1984).

[15] H. Ebert, J. Minar, and V. Popescu, in: *Band Ferromagnetism*; edited by K. Baberschke, M. Donath, and W. Nolting (Springer-Verlag, Berlin, 2001), p. 371.

[16] R. N. Zare, *Angular Momentum* (Wiley, New York, 1988).

[17] D. T. Pierce and F. Meier, Phys. Rev. B **13**, 5484 (1976).

[18] [ ] C. S. Fadley, in: *Synchrotron Radiation Research: Advances in Surface and Interface Science*, R. Z. Bachrach, Ed. (Plenum Press, New York, 1992).

[19] Multiple scattering program for calculating photoelectron diffraction available at: http://csic.sw.ehu.es/jga/software/edac/index.html, with the methodology behind it described in F.J. Garcia de Abajo, M.A. Van Hove, and C.S. Fadley, Phys. Rev. B **63**, 075404 (2001).

[20] S. Tanuma, C. J. Powell, and D. R. Penn, Surf. Interface Anal. **37**, 1 (2005); S. Tanuma, C. J. Powell, and D. R. Penn, "*Calculations of electron inelastic mean free paths. IX. Data for 41 elemental solids over the 50 eV to 30 keV range*", to be published.

[21] R. Feder, in: *Polarized Electrons in Surface Physics*, ed. by R. Feder (World Scientific, Singapore, 1985).

[22] G. Borstel, Appl. Phys. A **38**, 193 (1985).

[23] A. Damascelli, Z. Hussain, and Z.-X. Shen, Rev. Mod. Phys. **75**, 473 (2003).

[24] A. Oelsner, O. Schmidt, M. Schicketanz, M.J. Klais, G. Schönhense, V. Mergel, O. Jagutzki, H. Schmidt-Böcking, Rev. Sci. Instrum. **72** (2001) 3968.

[25] N. Takahashi, F. Matsui, H. Matsuda, Y. Hamada, K. Nakanishi, H. Namba, and H. Daimon, J. Electron Spectr. Rel. Phen. **163**, 45 (2008).

[26] J. Kessler, *Polarized Electrons*, 2nd ed. (Springer-Verlag, Berlin, 1985).

[27] J. Kirschner, *Polarized Electrons at Surfaces*, Springer Tracts in Modern Physics Vol. 106 (Springer-Verlag, Berlin, 1985).

[28] L. Gregoratti, M. Marsi and M. Kiskinova, Synchr. Rad. News **12**, 40 (1999).

[29] M. Escher, N. Weber, M. Merkel, C. Ziethen, P. Bernhard, G. Schönhense, S. Schmidt, F. Förster, F. Reinert, B. Krömker, and D. Funnemann, J. Phys.: Condens. Matt. **17**, S1329 (2005).

[30] V. N. Strocov, R. Claessen, G. Nicolay, S. Hüfner, A. Kimura, A. Harasawa, S. Shin, A. Kakizaki, H. I. Starnberg, P. O. Nilsson, and P. Blaha, Phys. Rev. B **63**, 205108 (2001).

[31] available as pdf-file at `http://xdb.lbl.gov/`

[32] S. Doniach and M. Sunjic, J. Phys. C **3**, 285 (1970).

[33] E. Rotenberg, Advanced Light Source Berkeley, (priv. communication).

[34] S. V. Borisenko, M. S. Golden, S. Legner, T. Pichler, C. Dürr, M. Knupfer, J. Fink, G. Yang, S. Abell, and H. Berger, Phys. Rev. Lett. **84**, 4453 (2000).

[35] Y. J. Kim, C. Westphal, R. X. Ynzunza, Z. Wang, H. C. Galloway, M. Salmeron, M. A. Van Hove, C. S. Fadley, Surf. Sci. **416** (1998) 68.

[36] J. Osterwalder, A. Tamai, W. Auwarter, M.P. Allan, and T. Greber, Chimia **60** (2006) A795, and earlier references therein.

[37] A. Bailly, O. Renault, N. Barrett, T. Desrues, D. Mariolle, L. F. Zagonel, and M. Escher, J. Phys.: Condens. Matt. **21**, 314002 (2009).

[38] B. Kroemker, M. Escher, D. Funnemann, D. Hartung, H. Engelhard, and J. Kirschner, Rev. Sci. Instrum. **79**, 053702 (2008).

[39] E. Kisker, K. Schröder, W. Gudat, and M. Campagna, Phys. Rev. B **31**, 329 (1985).

[40] H. B. Rose, A. Fanelsa, T. Kinoshita, Ch. Roth, F. U. Hillebrecht, and E. Kisker, Phys. Rev. B **53**, 1630 (1996).

[41] E. Tamura and R. Feder, Europhys. Lett. **16**, 695 (1991).

[42] C. M. Schneider and J. Kirschner, Crit. Rev. Solid State Mater. Sci. **20**, 179 (1995).

[43] E. I. Rashba, Sov. Phys. Solid State **2**, 1109 (1960).

[44] S. LaShell, B. A. McDougall and E. Jensen, Phys. Rev. Lett. **77**, 3419 (1996).

[45] F. Reinert, J. Phys.: Condens. Matt. **15**, S693 (2003).

[46] W. Kuch and C. M. Schneider, Rep. Prog. Phys. **64**, 205 (2001).

[47] C. Bethke, E. Kisker, N. B. Weber, and F. U. Hillebrecht, Phys. Rev. B **71**, 024413 (2005).

[48] D. Venus, Phys. Rev. B **43**, 6144 (1993).

[49] F. Manghi, V. Bellini, J. Osterwalder, T. J. Kreutz, and P. Aebi, C. Arcangeli, Phys. Rev. B **59**, R10409 (1999).

[50] K. Ono, K. Shimada, Y. Saitoh, T. Sendohda, A. Kakizaki, T. Ishii, and K. Tanaka, J. Electron Spectr. Rel. Phen. **78**, 325 (1996).

[51] Y. Sakisaka, T. Komeda, M. Onchi, H. Kato, S. Masuda, and K. Yagi, Phys. Rev. B **36**, 6383 (1987).

[52] F. Manghi, V. Bellini, and C. Arcangeli, Phys. Rev. B **56**, 7149 (1997).

[53] R. Clauberg, W. Gudat, E. Kisker, E. Kuhlmann, and G. M. Rothberg, Phys. Rev. Lett. **47**, 1314 (1981).

[54] G. Grimvall, *The Electron-Phonon Interaction in Metals*, Selected Topics in Solid State Physics, edited by E. Wohlfarth (North-Holland, New York, 1981).

[55] S.-J. Tang, J. Shi, B. Wu, P. T. Sprunger, W. L. Yang, V. Brouet, X. J. Zhou, Z. Hussain, Z.-X. Shen, Z. Zhang, and E. W. Plummer, phys. stat. sol. (b) **241**, 2345 (2004).

[56] K. Kobayashi, Nucl. Instrum. Methods A **601**, 32 (2009).

[57] R. Waser and M. Aono, Nat. Mater. **6**, 833 (2007).

[58] H. Kumigashira (priv. communication).

[59] R. Meservey and P. M. Tedrow, Phys. Rep. **238**, 173 (1994).

[60] G.-X. Miao, M. Münzenberg, and J. S. Moodera, Rep. Prog. Phys. **74**, 036501 (2011).

[61] C. Caspers, M. Müller, A. X. Gray, A. M. Kaiser, A. Gloskovskii, C. S. Fadley, W. Drube, and C. M. Schneider, Phys. Status Solidi RRL **1**, 1 (2011).

[62] L. Plucinski, J. Minar, B. C. Sell, J. Braun, H. Ebert, C. M. Schneider, and C. S. Fadley, Phys. Rev. B **78**, 035108 (2008).

[63] F. Venturini, J. Minar, J. Braun, H. Ebert, and N. B. Brookes, Phys. Rev. B **77**, 045126 (2008).

[64] C. S. Fadley, J. Electron Spectr. Rel. Phen. **178–179**, 2 (2010).

[65] A. X. Gray, C. Papp, S. Ueda, B. Balke, Y. Yamashita, L. Plucinski, J. Minar, J. Braun, E. R. Ylvisaker, C. M. Schneider, W. E. Pickett, H. Ebert, K. Kobayashi, and C. S. Fadley, Nat. Mater. **10**, 759 (2011).

[66] S.-H. Yang, B. S. Mun, N. Mannella, S.-K. Kim, J. B. Kortright, J. Underwood, F. Salmassi, E. Arenholz, A. Young, Z. Hussain, M. A. Van Hove, and C. S. Fadley, J. Phys. Cond. Matt. **14**, L406 (2002).

[67] J. Woicik, Nucl. Instr. Meth. A **547**, 227 (2005).

[68] S.-H. Yang, B. S. Mun, N. Mannella, A. Nambu, B. C. Sell, S. B. Ritchey, F. Salmassi, S. S. P. Parkin, C. S. Fadley, J. Phys.: Condens. Matter **18**, L259 (2006).

[69] C. S. Fadley, S.-H. Yang, B. S. Mun, J. Garcia de Abajo, in: *Solid-State Photoemission and Related Methods: Theory and Experiment*, W. Schattke and M.A. Van Hove (Eds.), (Wiley-VCH Verlag GmbH, Berlin, 2003).

[70] S.-H. Yang, B.S. Mun, and C.S. Fadley, Synchrotron Radiation News **24**, 17 (2004).

[71] W. Eberhardt and F. J. Himpsel, Phys. Rev. B **21**, 5572 (1980).

[72] M. Wöhlecke and G. Borstel, Phys. Rev. B **24**, 2857 (1981); M. Wöhlecke and G. Borstel, Phys. Rev. B **23**, 980 (1981); G. Borstel and M. Wöhlecke, Phys. Rev. B **24**, 2321 (1981).